

Dense gas and star formation in the Outer Milky Way

J. Braine¹, Yan Sun², Y. Shimajiri³, F.F.S. van der Tak^{4,5}, Min Fang², Ph. André⁶, Hao Chen⁷, and Yu Gao^{8,2}

¹ Laboratoire d'Astrophysique de Bordeaux, Univ. Bordeaux, CNRS, B18N, allée Geoffroy Saint-Hilaire, 33615 Pessac, France
e-mail: jonathan.braine@u-bordeaux.fr

² Purple Mountain Observatory, Chinese Academy of Sciences, 10 Yuanhua Road, Nanjing 210023, China

³ Kyushu Kyoritsu University, Jiyugaoka 1-8, Yahatanishi-ku, Kitakyushu, Fukuoka, 807-8585, Japan

⁴ SRON Netherlands Institute for Space Research, Landleven 12, 9747 AD Groningen, The Netherlands

⁵ Kapteyn Astronomical Institute, University of Groningen, NL

⁶ Laboratoire d'Astrophysique (AIM), CEA/DRF, CNRS, Université Paris-Saclay, Université Paris Diderot, Sorbonne Paris-Cité, 91191 Gif-sur-Yvette, France

⁷ Research Center for Intelligent Computing Platforms, Zhejiang Laboratory, Hangzhou 311100, China

⁸ Department of Astronomy, Xiamen University, Xiamen, Fujian 361005, China

Received xxxx; accepted xxxx

ABSTRACT

We present maps and spectra of the HCN(1–0) and HCO⁺(1–0) lines in the extreme outer Galaxy, at galactocentric radii between 14 and 22 kpc, with the 13.7 meter Delingha telescope. The 9 molecular clouds were selected from a CO/¹³CO survey of the outer quadrants. The goal is to better understand the structure of molecular clouds in these poorly studied subsolar metallicity regions and the relation with star formation. The lines are all narrow, less than 2 km s^{−1} at half power, enabling detection of the HCN hyperfine structure in the stronger sources and allowing us to observationally test hyperfine collision rates. The hyperfine line ratios show that the HCN emission is optically thin with column densities estimated at $N(\text{HCN}) \approx 3 \times 10^{12} \text{ cm}^{-2}$. The HCO⁺ emission is approximately twice as strong as the HCN (taken as the sum of all components), in contrast with the inner Galaxy and nearby galaxies where they are similarly strong. For an abundance ratio $\chi_{\text{HCN}}/\chi_{\text{HCO}^+} = 3$, this requires a relatively low density solution for the dense gas, with $n(\text{H}_2) \sim 10^3 - 10^4 \text{ cm}^{-3}$. The ¹²CO/¹³CO line ratios are similar to solar neighborhood values, roughly 7.5, despite the low ¹³CO abundance expected at such large radii. The HCO⁺/CO and HCO⁺/¹³CO integrated intensity ratios are also standard at about 1/35 and 1/5 respectively. The HCN is weak compared to the CO emission, with HCN/CO $\sim 1/70$ even after summing all hyperfine components. In low-metallicity galaxies, the HCN deficit is attributed to a low [N/O] abundance ratio but in the outer disk clouds it may also be due to a low volume density. At the parsec scales observed here, the correlation between star formation, as traced by 24 μm emission as is standard in extragalactic work, and dense gas via the HCN or HCO⁺ emission, is poor, perhaps due to the lack of dynamic range. We find that the lowest dense gas fractions are in the sources at high galactic latitude ($b > 2^\circ$, $h > 300 \text{ pc}$ above the plane), possibly due to a lower pressure.

Key words. Galaxies: Individual: Milky Way – Galaxies: ISM – ISM: clouds – ISM: Molecules – Stars: Formation

1. Introduction

A general theory of star formation needs to be tested in multiple environments. Most work (see e.g. Kennicutt & Evans 2012) has studied either galactic disk star formation, star formation in bright and perturbed environments such as mergers or ULIRGs, or bright low metallicity objects such as blue dwarf galaxies. Observations of the outer Galaxy provide a new environment for the study of the star formation cycle (H I to H₂ to stars). The outer disk is cooler and has a lower gas content and in particular less molecular gas than the brighter regions mentioned above. The star formation rate is low (see e.g. Sodroski et al. 1997) and the metallicity is subsolar but not extremely low in the outer disk (gradient of $\approx 0.04 \text{ dex kpc}^{-1}$, Pedicelli et al. 2009). The morphology and gravitational potential are those of a rotating disk, unlike mergers and many dwarfs. Finally, the outer disk, defined as beyond the R₂₅ radius, is typically where the gas surface density exceeds that of stars (see e.g. Figure 7 of Kennicutt & Evans (2012) or Figure 1 of Hoekstra et al. (2001)). For a population of sun-like stars, a brightness of 25 magnitudes per square arcsecond, defining the R₂₅ radius, corresponds to a stellar surface density of $6.6 \text{ M}_\odot \text{ pc}^{-2}$. Hence, the outer Galaxy represents a new

environment (where $\Sigma_{\text{gas}} \gtrsim \Sigma_*$) for the study of the star formation cycle.

A further motivation comes from the observations and simulations showing that galaxies continue to be fueled by inflowing gas (see Linsky 2003; Schmidt et al. 2016, and references therein), particularly when a bar (i.e. a non-axisymmetric potential) is present as is the case for the Galaxy. Thus the outer disk represents a part of the future of our Galaxy.

The star formation rate (hereafter SFR) at kpc scales is well-known to be linked to the presence of gas and particularly molecular gas (e.g. Kennicutt 1989). Closer to cloud scales, the cloud life-cycle (pre-SF, embedded SF, exposed SF, cloud dispersal) is such that much more scatter is present in the SFR-H₂ relation. More recently, the link between the dense gas mass, generally as traced by the high-dipole moment molecules HCN or HCO⁺, has been shown to be approximately linear in galactic disks at both kpc (e.g. Gao & Solomon 2004b,a; Kepley et al. 2014; Chen et al. 2017; Braine et al. 2017) and pc scales (e.g. Wu et al. 2010; Shimajiri et al. 2017) with approximately the same SFR/M_{gas} ratio (see Fig. 13 of Jiménez-Donaire et al. 2019). In galactic centers, the SFR/M_{gas} ratio is clearly lower than in disks (see lower panel of Fig. 7

in Chen et al. 2015; Usero et al. 2015). Table 5 and Figure 13 of Jiménez-Donaire et al. (2019) show that over about 10 orders of magnitude in L_{HCN} , there is a scatter of 0.37 dex in the $L_{\text{IR}}/L_{\text{HCN}}$ ratio, where L_{IR} traces the SFR, in agreement with Gallagher et al. (2018).

IRAS Far-IR observations and the follow-up in CO by Wouterloot & Brand (1989) revealed molecular gas out to a galactocentric distance of about 18 kpc. Perhaps surprisingly, Digel et al. (1994) found several molecular clouds beyond 18 kpc but they are all much less CO-bright (although of comparable mass) than Orion viewed at a similar distance and resolution. The atomic gas extends considerably further (e.g. Kalberla & Kerp 2009) but with little or no evidence of star formation and young stars.

Recent increases in mapping speed and receiver bandwidth combined with post-IRAS Far-IR surveys such as Herschel Hi-Gal (Molinari et al. 2016) and the APEX Atlasgal (Schuller et al. 2009) has led to revived interest in the outer Galaxy. Sun et al. (2015) surveyed a vast region covering $100 < l < 150^\circ$ and $-3 < b < 5.25^\circ$ in the $J = 1 - 0$ transition of CO and isotopologues to determine how much molecular gas is present at large galactocentric distances. In addition to previously known clouds, they found 49 previously undetected extreme outer Galaxy clouds ($R_{\text{gal}} > 14\text{kpc}$). The CO emission is generally quite weak, with integrated intensities below 10 K km s^{-1} at the CO peaks. $^{13}\text{CO}(1-0)$ and $\text{C}^{18}\text{O}(1-0)$ were observed simultaneously and the images and spectra are presented in Sun (2015). $^{13}\text{CO}(1-0)$ emission is detected in nearly half of the sources. The $^{12}\text{CO}/^{13}\text{CO}$ line ratio is typically about 5 in peak temperature and 7 in integrated intensity; the C^{18}O lines were not detected (see Sect. 4.1).

Sun (2015) started a comparison between star formation and the presence of molecular gas in the outer Galaxy. One of the results of her thesis was that while star formation was not always associated with molecular gas in these extreme outer Galaxy clouds, the clouds hosting young stellar objects (YSOs) were generally more massive than those without YSOs. Here we pursue the comparison between tracers of star formation and molecular gas in the outer Galaxy, focussing on the link between *dense* gas and star formation. At kpc scales, there is a good correlation between the dense gas mass and the star formation rate (Chen et al. 2015) as for whole galaxies (Gao & Solomon 2004b). The low- J transitions of the high dipole moment molecules HCN and HCO^+ are standard tracers of dense gas because high densities (close to 10^5 cm^{-3}) are required for collisional excitation (Evans 1999). However, the lines are much (factor 10–100) weaker than the CO lines so the existing $^{12}\text{CO}(1-0)$ and $^{13}\text{CO}(1-0)$ observations were used to define regions to be observed in HCN and HCO^+ in the extreme outer Galaxy. The dataset obtained is used to explore the physical conditions of the molecular medium far out in the Galaxy and the link between dense gas and star formation in a new environment (e.g. Glover & Clark 2012). There is evidence that HCN is more sensitive to metallicity variations than HCO^+ (Rudolph et al. 2006; Nishimura et al. 2016; Braine et al. 2017). The outer Galaxy has a subsolar metallicity but also a generally weak UV field and thus provides complementary information to observations of low metallicity galaxies, which often have high UV-fields.

Only a few observations of dense gas tracers in the outer Galaxy have been made (Yuan et al. 2016) so we significantly increase this sample. Yuan et al. (2016) observed a large sample of Planck Galactic Cold Clumps, detected in the sub-mm range by the Planck satellite and generally close to the Sun. The sam-

ples are quite different in that the Sun et al. (2015) survey was blind and *none* of their 72 sources were detected in the C^{18}O line. Very recently, Fontani et al. (2022) observed molecular lines, including HCN and HCO^+ , in a sample of actively star-forming IRAS-selected cores and Patra et al. (2022) mapped the HCN and $\text{HCO}^+(1-0)$ lines around regions with massive stars, also in the outer Galaxy. These two samples are quite different from ours, as we will see (Sect. 4.2).

The paper is structured as follows: after presenting the observations and the basic results, we estimate the excitation temperatures, optical depths, and column densities of the CO lines and then for the HCN, where the satellite line strengths are used to estimate the optical depth. In this part, we initially follow Yuan et al. (2016). The following section presents radiative transfer calculations of the HCN line ratios and also the HCN/ HCO^+ line ratio, in order to constrain the volume density and determine whether the CO-emitting gas can also be responsible for the HCN and HCO^+ line emission. We then discuss, with in particular the goal of understanding why the line ratios we measure are not typical of galactic or most extragalactic observations, and summarize the results for this rather unique data set.

2. Cloud sample and Observations

The sources were selected from the Sun et al. (2015) sample of outer Galaxy CO clouds. All of the clouds are quite far from the galactic center, ranging from 14 to 22 kpc with the Reid et al. (2014) rotation curve. Although a different rotation curve will yield slightly different results, these are clearly far outer Galaxy objects, close to or beyond twice the solar circle distance. Sources were chosen to have (a) an integrated CO($1-0$) intensity $I_{\text{CO}} > 7\text{ K km s}^{-1}$ and (b) $I_{^{13}\text{CO}} \geq 1.4\text{ K km s}^{-1}$ and (c) a peak ^{13}CO temperature above 0.7 Kelvin. The ^{13}CO data are from Sun (2015) and the cloud characteristics, ^{12}CO , and ^{13}CO intensities are provided in Table 1. This yielded a sample of nine clouds: 7, 14, 16, 18, 21, 30, 34, 56 and 57, all of which have ^{13}CO sizes between 2 and 5 square arcminutes and peak CO temperatures above 4 Kelvins. The central positions of all clouds were observed and clouds 21, 56, and 57, the brightest in HCN and HCO^+ , were mapped. Fig. 1 presents WISE 22 μm band images, supposed to trace star formation, with the positions observed and symbols indicating class I and class II YSOs. Fig. 2 shows the same for the three clouds that were mapped in HCN and HCO^+ along with contours of CO intensity. The WISE 22 μm band¹ was chosen as it was the only tracer of star formation available for all sources.

The YSOs within the clouds were identified with the criteria described in Koenig et al. (2012) using the infrared data from the Two Micron All Sky Survey (2MASS: Skrutskie et al. 2006) and the Wide-field Infrared Survey Explorer (WISE: Wright et al. 2010). We restrain our sources to those with photometric errors less than 0.1 mag for 2MASS data and signal-to-noise ratio greater than 5 for WISE data. The criteria in Koenig et al. (2012) are designed to search for young stars at Class I and Class II stages employing two methods. The first is based on photometry in the WISE 3.4, 4.6 and 12 μm bands. The contamination from extragalactic sources (star-forming galaxies and AGNs), shock emission blobs, resolved PAH emission objects can be removed according to their locations in the [3.4]–[4.6] vs. [4.6]–[12] color-color diagram and their WISE photometry. For the sources not detected in the WISE 12 μm band, YSOs are

¹ <https://irsa.ipac.caltech.edu/Missions/wise.html>

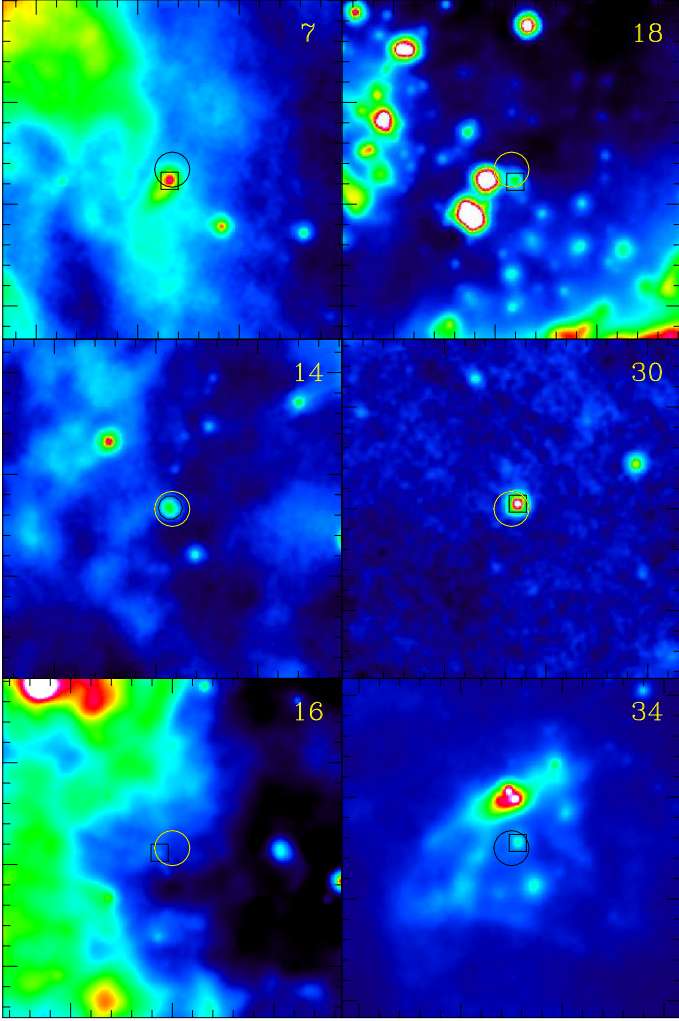


Fig. 1. WISE 22 μm band images of sources 7, 14, 16, 18, 30, and 34 (identification in upper right corner). These are the sources for which only a single pointing is available. The images are all 10 arcminutes in size, oriented in l and b . The central circle gives the HCN/HCO⁺ beamsize. The transfer function (rainbow from black to white) of the WISE observations differs from image to image. For cloud 7 it is from 91.5 to 98; for cloud 14 it is 100.5 to 107; for 16 it is 103 to 115; for 18 it is 102 to 114; for 30 it is from 108 to 112 and for cloud 34 it is from 108 to 135 counts. Following Sun (2015), class I sources within our maps are shown as circles and class II as squares.

identified from the dereddened $K_s - [3.4]$ vs. $[3.4] - [4.6]$ color-color diagram. In our work, the extinction used to deredden the photometry is estimated from its location in the $J - H$ vs. $H - K_s$ color-color diagram as described in Fang et al. (2013).

The nominal central positions observed correspond to the CO maxima and not necessarily a peak in star formation, as can be seen in Figures 1 and 2. Below we give the assessment of the star formation for each observed region (Sun 2015), starting with the single positions and followed by the maps.

Cloud 7: An IRAS point source is present as well as a class II source within the DLH beam.

Cloud 14: No IRAS point source within the beam but a class I source at beam center.

Cloud 16: No IRAS point source but there is a class II source within the DLH beam.

Cloud 18: No IRAS point source but there is a class II source within the DLH beam.

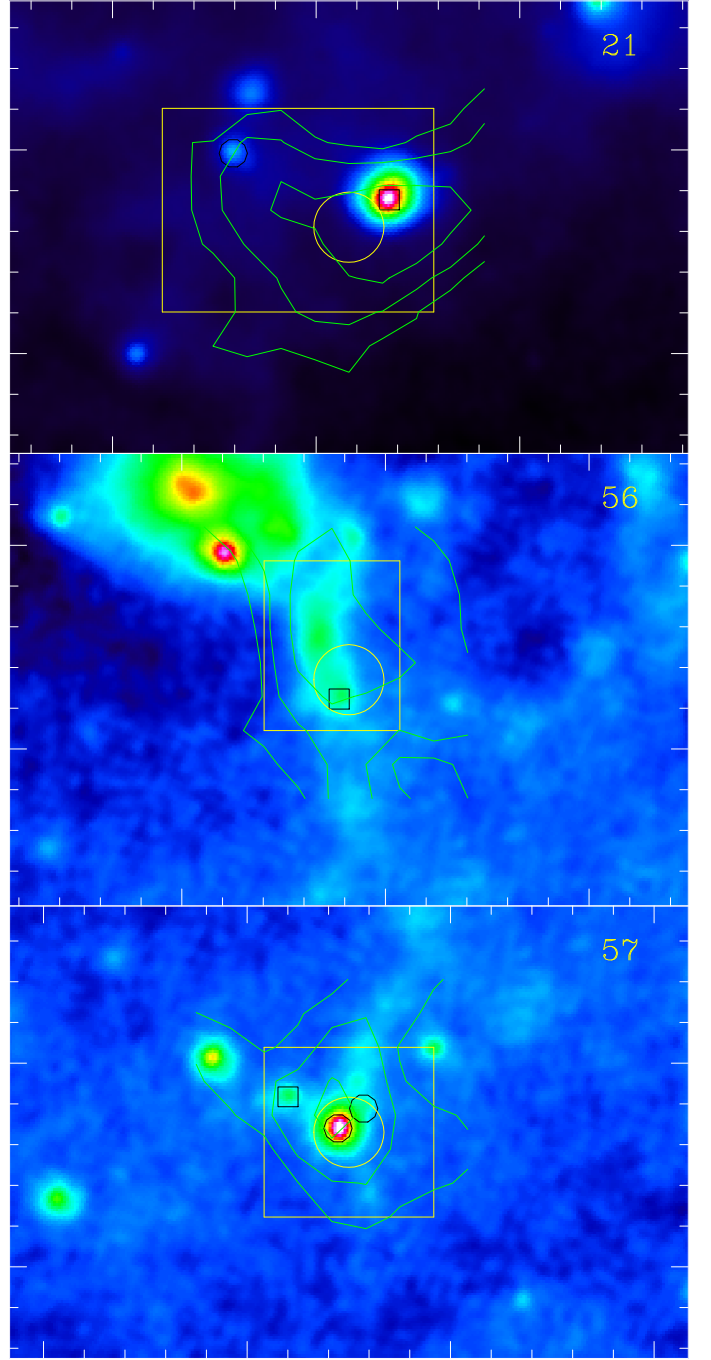


Fig. 2. WISE 22 μm band images of sources 21, 56, and 57 (identification in upper right corner). These are the sources which were mapped. The images are all 600'' \times 400'' in size, oriented in l and b . The color scale (rainbow from black to white) of the WISE observations differs from image to image. For cloud 21 it is from 95 to 116 and for clouds 56 and 57 the range is from 129 to 134 counts. The central circle gives the HCN/HCO⁺ beamsize and is the (0,0) position in Figures 4, 5, and 6 which show the spectra. The box indicates the size of the region shown in Figures 4, 5, and 6. Following Sun (2015), class I sources within our maps are shown as circles and class II as squares.

Cloud 30: No IRAS point source but there is a class II source within the DLH beam.

Cloud 34: Class II source within DLH beam and IRAS source nearby (see Fig. 1).

Cloud 21: IRAS point source and class II source at edge of central beam but within map, which also covers a class I source.

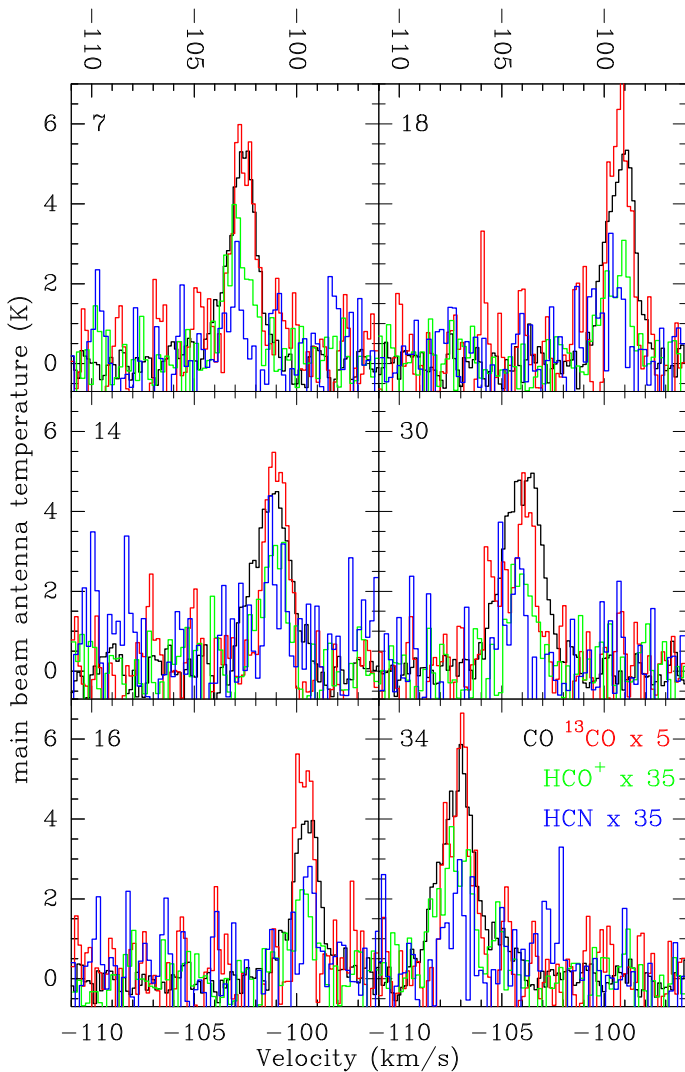


Fig. 3. Spectra for the clouds that have not been mapped, as in Fig. 1. The axes are the same for each cloud. ^{12}CO is in black and corresponds to the temperature scale. ^{13}CO is in red and has been multiplied by 5. HCO^+ , in green, has been multiplied by 35. The HCN spectra have been multiplied by 35 for comparison with HCO^+ but also multiplied by 9/5 to account for the satellite lines as explained in the text. The ^{12}CO and ^{13}CO spectra have been convolved with a gaussian kernel to the angular resolution of the HCN and HCO^+ spectra.

Map shows no obvious difference in line ratios at positions with star formation.

Cloud 56: No IRAS point source within but a class II source near nominal center. Star formation ($22\ \mu\text{m}$ emission) extends to higher b and HCN/ HCO^+ emission appears to follow.

Cloud 57: IRAS point source at center and two class I sources, one coincident with the IRAS source. A class II source is also present further from the center.

Class I sources are indicated as circles in Figures 1 and 2. Class II are shown as squares, following Sun (2015).

The observations were carried out in May 2017 with the 13.7m telescope of the Purple Mountain Observatory (PMO) in Delingha, Qinghai, China, hereafter DLH. The beamsize at the HCN and $\text{HCO}^+ J = 1 - 0$ frequencies is $1'$ which corresponds to a linear scale of 3 pc at the typical distance of 10 kpc of our clouds (except clouds 56 and 57 which are further such that the beam size is about 4.3 pc). The Superconducting Spectroscopic Array Receiver system, a nine-beam (3X3beam, with separation

Cloud #	l °	b °	I_{CO} K km s $^{-1}$	R_{gal} (kpc)	dist (kpc)	$I_{^{13}\text{CO}}$ K km s $^{-1}$
7	104.983	3.317	11.4	14.5	9.9	1.6
14	109.292	2.083	11.5	14.6	9.5	1.7
16	109.500	2.608	7.4	14.5	9.3	1.4
18	109.792	2.717	10.3	14.4	9.2	1.8
21	114.342	0.781	18.0	15.0	9.5	2.4
30	121.817	3.050	13.7	16.4	10.3	2.0
34	122.775	2.525	12.8	17.1	11.0	1.9
56	137.759	-0.983	17.6	21.7	14.7	3.1
57	137.775	-1.067	12.2	21.4	14.4	1.6

Table 1. Cloud sample: source numbers, positions, ^{12}CO intensities, galactocentric distance R_{gal} , heliocentric distance, all from Sun et al. (2015), and ^{13}CO intensities from Sun (2015).

of 3 arcmin), sideband- separating receiver (Shan et al. 2012) was used as front end. The fast fourier transform spectrometer with a bandwidth of 1 GHz provides 16384 channels and a spectral resolution of 61 kHz (see details in Shan et al. 2012), leading to a velocity resolution of $0.2\ \text{km s}^{-1}$. The telescope is at an altitude of 3200 meters and the weather was good during the observations, leading to system temperatures of 140 – 150K.

The standard chopper-wheel calibration was adopted to obtain the antenna temperature, T_{A}^* (Kutner & Ulich 1981). Spectral intensities are further converted to a scale of main-beam brightness temperature using $T_{\text{MB}} = T_{\text{A}}^*/\eta_{\text{MB}}$, where the main-beam efficiency η_{MB} is 0.57 at $\sim 90\ \text{GHz}$ (see the status report of the 13.7m telescope²). Considering the small angular size of our targets traced by CO, and the smaller region traced by dense gas, the position-switching mode was used. Two beams with a separation of 6 arcmin were used to observe on-source pointing and emission-free OFF position simultaneously. The pointing accuracy is estimated to be better than 5 arcsec. The mapping step is 30 arcsec.

3. Results

3.1. Maps and Spectra

Table 1 provides source numbers, positions, ^{12}CO intensities, galactocentric distance R_{gal} , heliocentric distance, all from Sun et al. (2015), and ^{13}CO intensities from Sun (2015). The CO data are on the main beam scale (i.e. corrected for telescope efficiency) and come from observations with the Delingha telescope which has a beam size of $48''$ at the CO(1–0) frequency.

In Galactic observations, several clouds can be found along the line of sight at different velocities. More common in the inner Galaxy, this is also the case for these outer Galaxy observations. The outer Galaxy CO survey (Sun et al. 2015; Sun 2015) covered not only the peaks but a vast region in the outer Galaxy and thus maps of each cloud. The spectra and maps of the clouds in the appendix of Sun (2015) show that generally the CO and ^{13}CO is strongest in the distant cloud we are interested in and that even when this is not the case (only cloud 30), the clouds can be visually separated in the maps.

The new observations of the HCN(1–0) and $\text{HCO}^+(1–0)$ lines are shown along with the pre-existing $^{12}\text{CO}(1–0)$ and $^{13}\text{CO}(1–0)$ lines in Figures 3, 4, 5, and 6. The temperature scales are the same from one figure to another so that the figures can be straightforwardly compared. We immediately see that the HCN(1–0) and $\text{HCO}^+(1–0)$ lines were detected in all sources

² <http://english.dlh.pmo.cas.cn/fs/>

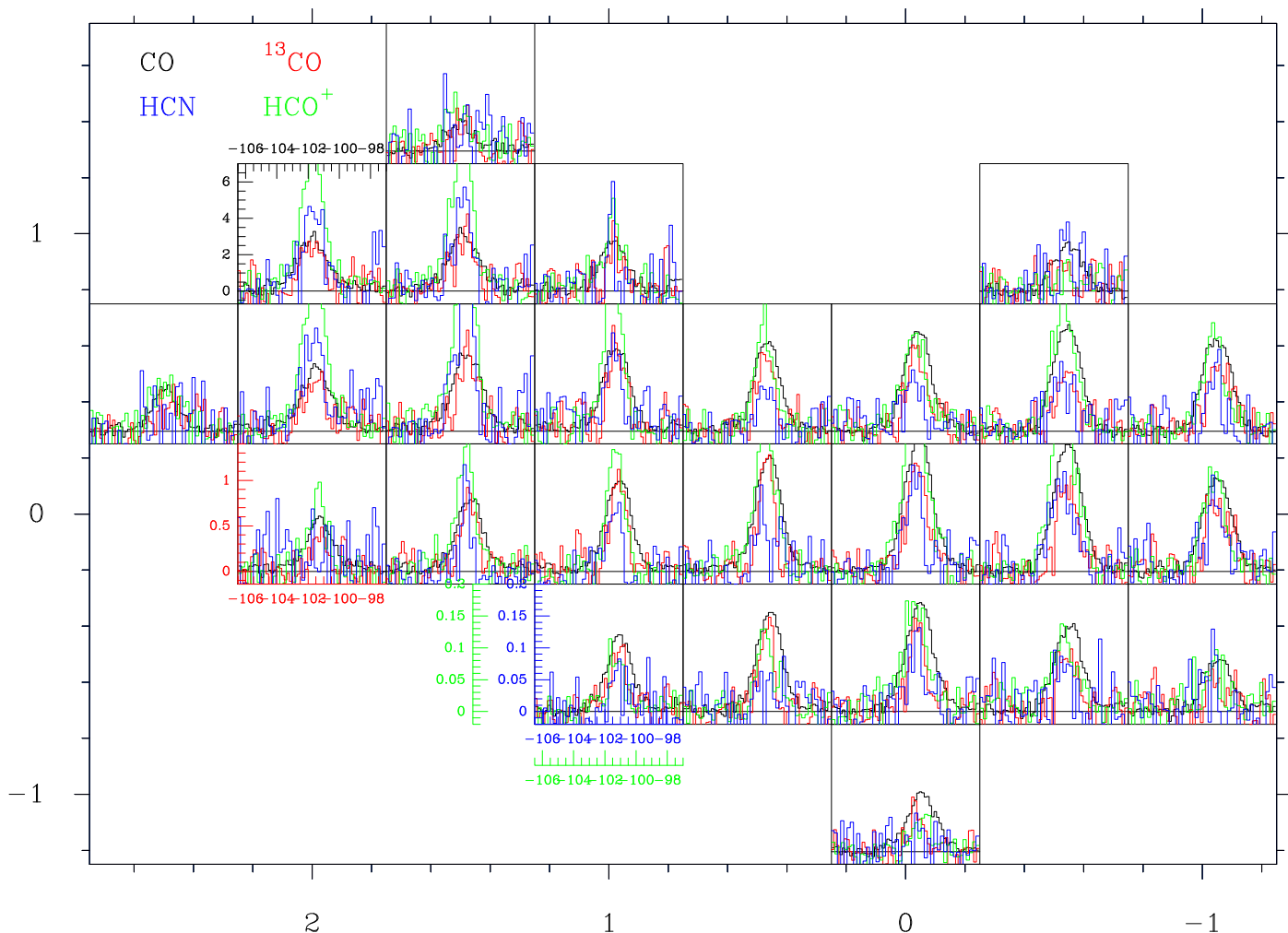


Fig. 4. Spectra of Cloud 21. Positions are indicated on the x and y axes as offsets in arcminutes and each box represents $30''$. ^{12}CO is in black, ^{13}CO in red, HCO^+ in green and HCN in blue. The velocity scale goes from -106.5 km s^{-1} to -97 km s^{-1} . The temperatures scales are -7 to 7K for ^{12}CO , -14 to 1.4K for ^{13}CO , -0.2 to 0.2 for HCO^+ and for HCN . The HCN line (only central component shown) has been multiplied by $9/5$ so that the line intensity represents the total line flux for comparison with other species. The ^{12}CO and ^{13}CO spectra have been convolved to the same angular resolution as the HCN and HCO^+ .

and that the HCO^+ line is systematically stronger than the HCN line. Central velocities are very similar (generally \pm one channel) and the optically thick ^{12}CO line is generally broader (by $\sim 40\%$) than the dense gas tracers (compare Table 2 with Table 1 of Sun et al. 2015).

Table 2 presents the results of the HCN and HCO^+ observations. The integrated intensity, velocity, and line width are given for the central spectra in the $\text{HCO}^+(1-0)$ line and for the main line of $\text{HCN}(1-0)$. Clouds 21, 56, and 57 were partially mapped in HCN and HCO^+ and the lines indicated by *sum* are the fits to the co-added (i.e. summed) spectra. The summed spectra have considerably higher signal-to-noise ratios (see last column) so the individual hyperfine components were fit and the results are presented in the same way.

3.2. HCN hyperfine structure

HCN and HCO^+ are considered to be tracers of dense gas due to their high electric dipole moment. Their critical densities, where collisional de-excitation equals spontaneous de-excitation (see Eq. 4 and Table 1 of Shirley 2015), are $n_{\text{crit},\text{HCN}(1-0)} \approx 4 \times 10^5 \text{ cm}^{-3}$ and $n_{\text{crit},\text{HCO}^+(1-0)} \approx 6 \times 10^4 \text{ cm}^{-3}$. These densities are

roughly 2 orders of magnitude higher than for CO so the typical molecular cloud densities at which CO is collisionally excited do not suffice to generate detectable HCN or HCO^+ emission. The outer galaxy environment is cool, with a weak radiation field, and as we shall see the HCN lines are optically thin or nearly so.

Due to the nuclear quadrupole moment of Nitrogen (^{14}N), there is hyperfine structure which is observable in the ground-state rotational transition ($J = 1 \rightarrow 0$). Three lines are present and the line ratios can be used to estimate optical depth. The main line is the $F = 2 \rightarrow 1$ transition at 88.63185 GHz , with satellite lines $F = 1 \rightarrow 1$ and $F = 0 \rightarrow 1$ shifted by respectively 4.8 and -7 km s^{-1} . Figure 7 shows the co-added $\text{HCN}(1-0)$ spectra for clouds 21, 56, and 57. The individual spectra do not have a sufficiently high signal-to-noise ratio to measure the HFS at individual positions, particularly for the weakest component. The spectra are presented for each cloud separately in Figures 4, 5, and 6, which show that the co-added spectra are from regions with strong CO (and ^{13}CO) emission. The second-strongest component is clearly visible in the individual spectra of cloud 56 (Fig. 5) which has the lowest noise level (see Table 2). Generally, when spectra are stacked, the velocity is recentered because the stacking concerns gas at different velocities – this shifting introduces additional uncertainties because of the

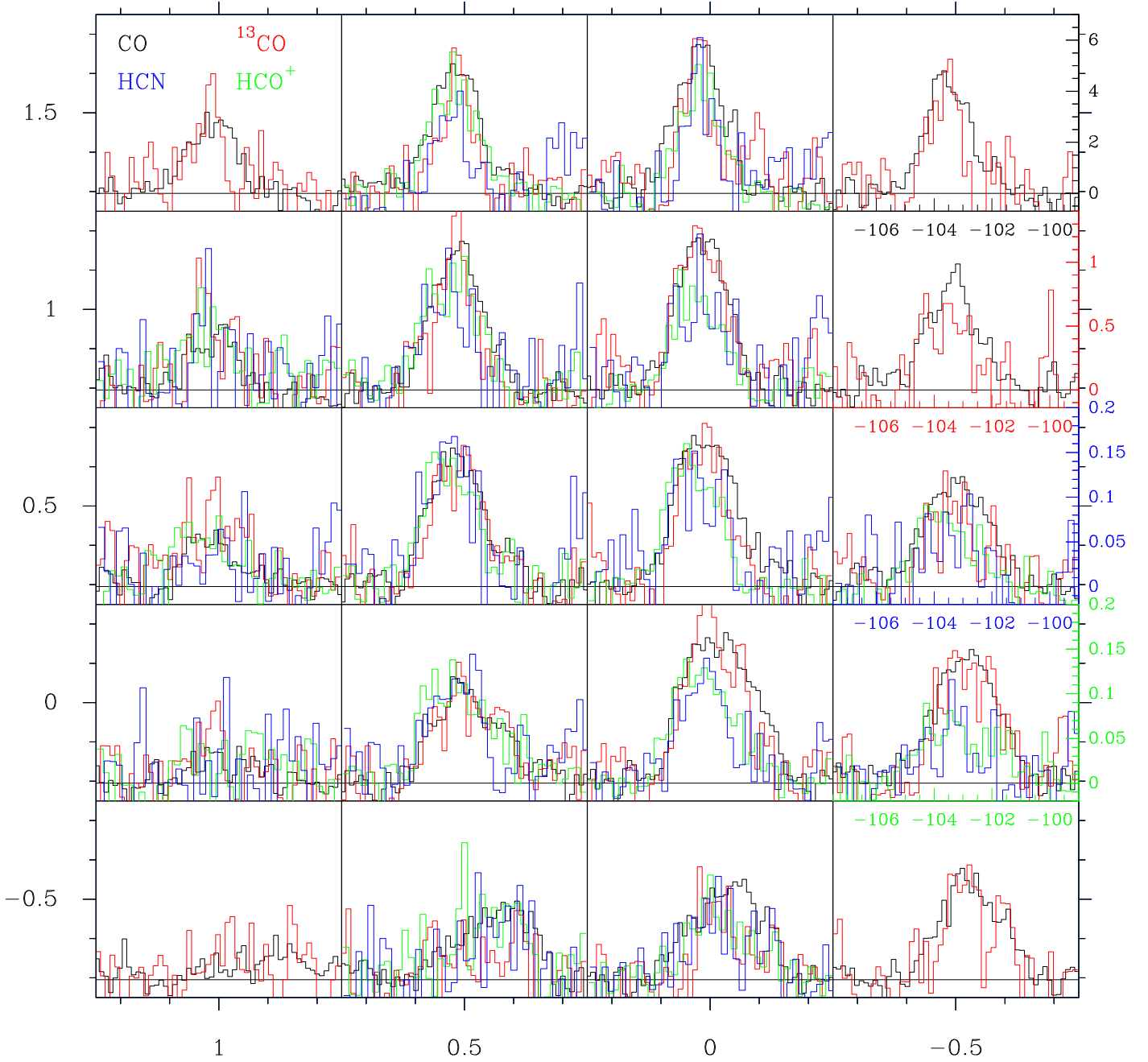


Fig. 5. Spectra of Cloud 56. Positions are indicated on the x and y axes as offsets in arcminutes and each box represents $30''$. ^{12}CO is in black, ^{13}CO in red, HCO^+ in green and HCN in blue. The velocity scale goes from -107.5 km s^{-1} to -99 km s^{-1} . The temperatures scales are -7 to 7K for ^{12}CO , -14 to 1.4K for ^{13}CO , -0.2 to 0.2 for HCO^+ and for HCN . The HCN line (only central component shown) has been multiplied by $9/5$ so that the line intensity represents the total line flux for comparison with other species. The spectra in the corners show only CO as not all positions were observed in HCN and HCO^+ .

way the velocity difference is determined. This is not the case here which is why we say “summed” or “co-added” rather than stacked.

3.3. Relative line intensities

As can be seen in Figures 9 and 10, the CO and ^{13}CO , and HCN and HCO^+ line fluxes are correlated. The relation is approximately $I_{\text{HCO}^+} \approx 0.03 I_{\text{CO}} \approx 0.21 I_{^{13}\text{CO}} \approx 2 I_{\text{HCN}}$ for the set of data. The correlation coefficients are $r = 0.62$ between dense gas tracers and $r = 0.65$ between the ^{12}CO and ^{13}CO lines. Mixing the dense and total gas tracers, for respectively CO-HCO^+ ,

CO-HCN , $^{13}\text{CO-HCO}^+$, and $^{13}\text{CO-HCN}$, the correlation coefficients are 0.53 , 0.44 , 0.44 , and 0.43 . Hence, the total gas mass (clouds) and dense gas mass (cores) are linked but the dense gas tracers (HCN , HCO^+) are more strongly correlated between each other, as are the general molecular gas tracers (CO , ^{13}CO), than between clouds and cores.

4. Physical conditions from an LTE analysis

In this section we apply the standard formulae to estimate optical depths and column densities of the species presented here. The formulae are presented in Yuan et al. (2016), Mangum & Shirley

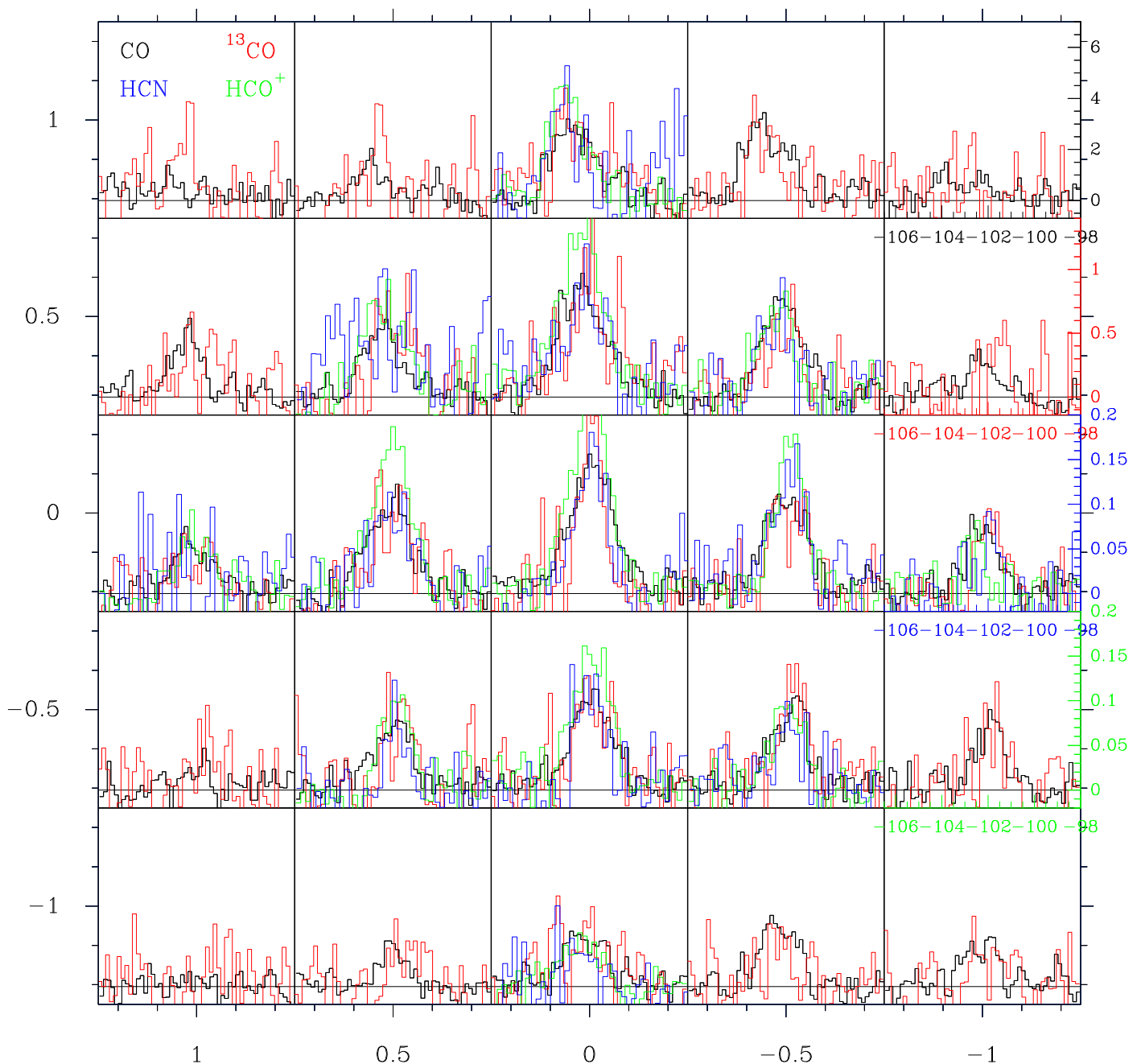


Fig. 6. Spectra of Cloud 57. Positions are indicated on the x and y axes as offsets in arcminutes and each box represents $30''$. ^{12}CO is in black, ^{13}CO in red, HCO^+ in green and HCN in blue. The velocity scale goes from -106.5 km s^{-1} to -98 km s^{-1} . The temperatures scales are -7 to 7K for ^{12}CO , -14 to 1.4K for ^{13}CO , -0.2 to 0.2 for HCO^+ and for HCN . The HCN line (only central component shown) has been multiplied by $9/5$ so that the line intensity represents the total line flux for comparison with other species. The spectra in the corners show only CO as not all positions were observed in HCN and HCO^+ .

(2015), and Shirley (2015) and the works cited therein. We initially follow the reasoning in Yuan et al. (2016) for straightforward comparison and then present another approach. Without making ad hoc hypotheses, it is difficult to make non-LTE (local thermodynamic equilibrium) calculations so the following section presents radiative transfer calculations with RADEX (van der Tak et al. 2007).

The observations are of clouds between 14 and 22 kpc from the Galactic center so we expect abundances to be sub-solar (e.g. Pedicelli et al. 2009) and we follow the Pineda et al. (2013) $^{12/13}\text{C}$ gradient (see Eq. 4 in Yuan et al. 2016) and the

Fontani et al. (2012) ^{12}CO abundance gradient (see Eq. 7 in Yuan et al. 2016).

4.1. Molecular column densities: $^{12}\text{CO}(1-0)$ and $^{13}\text{CO}(1-0)$

Following Yuan et al. (2016) Eqs. 3 and 4, we estimate the $^{13}\text{CO}(1-0)$ optical depth, τ_{13} , and, multiplying by the $^{12/13}\text{C}$ ratio, the optical depth of the main line, τ_{12} . This assumes that excitation temperatures and surface filling factors (fraction of the beam occupied by emitting molecules) are the same for both isotopologues. The $^{13}\text{CO}(1-0)$ emission is optically thin, with $0.15 < \tau_{13} < 0.32$ calculated in this way, yielding main iso-

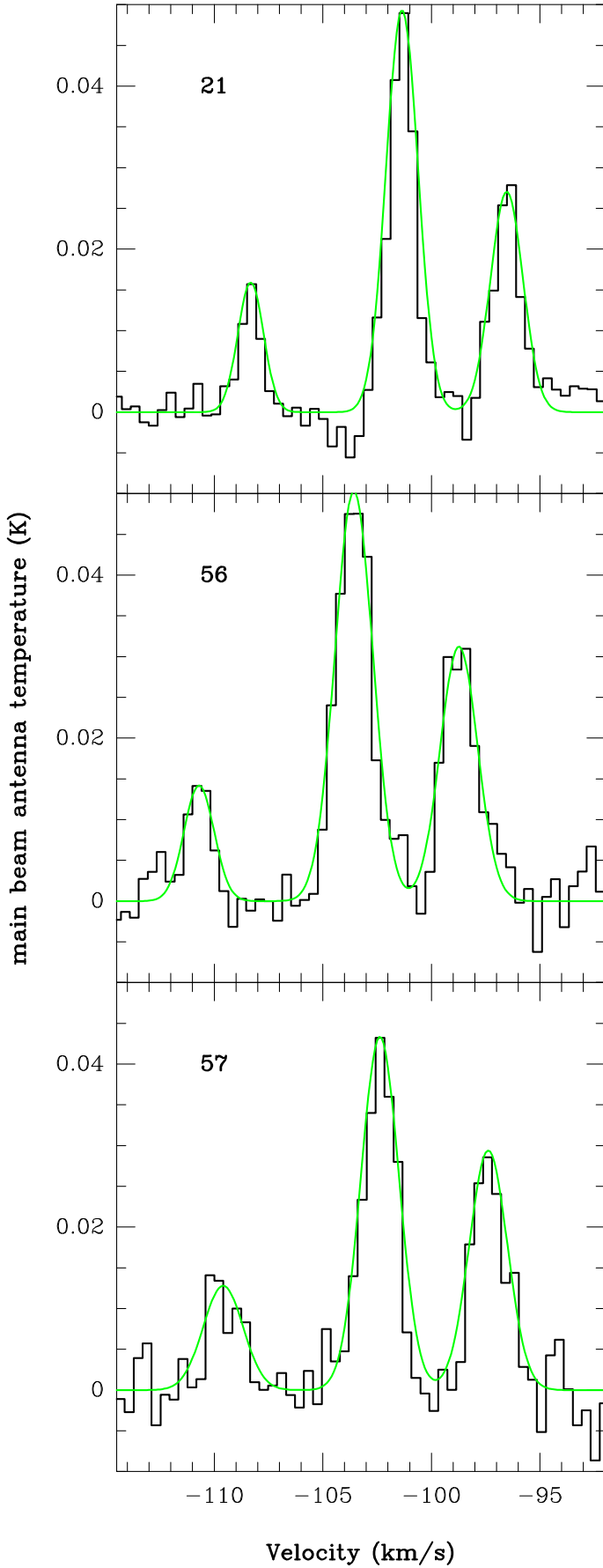


Fig. 7. Sum of spectra for each of the clouds for which we were able to make maps. The lines are narrow although each spectrum represents a sum of many positions. The clear separation of the hyperfine components enables us to estimate the optical depth. The parameters of the gaussian fits shown in green are given in Table 2.

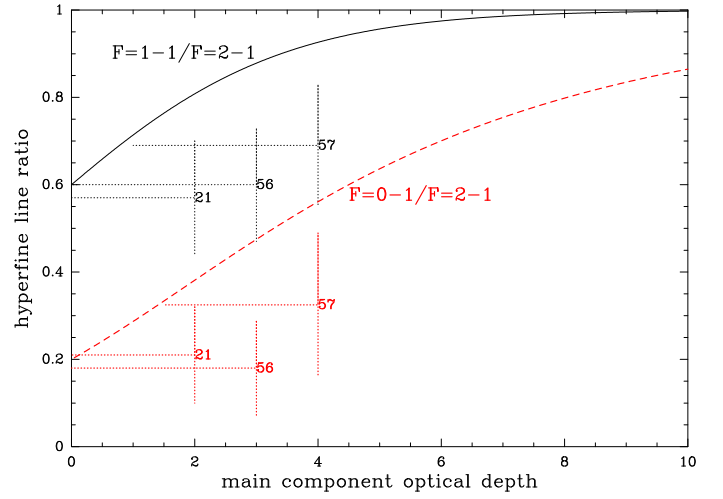


Fig. 8. Local Thermodynamic Equilibrium representation of hyperfine component ratios as a function of main component ($F=2-1$) optical depth. The observed ratios for clouds 21, 56, and 57 are indicated. The vertical dashed lines indicate the uncertainties from Table 3.

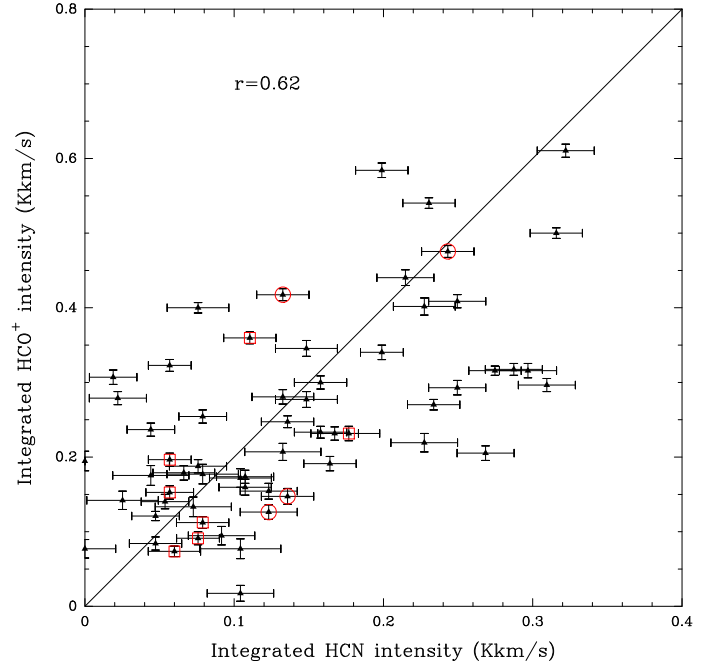


Fig. 9. Integrated intensities of HCN and HCO^+ lines for all positions observed. All data are on the main beam temperature scale and the central HCN intensity has been multiplied by 9/5 to account for the satellite hyperfine components. The line indicates $I_{\text{HCO}^+} = 2I_{\text{HCN}}$, close to the best-fit value of 1.92. Class I and II sources are indicated by respectively red circles and squares.

tope optical depths of order 20. $\text{C}^{18}\text{O}(1-0)$ emission was not detected in these sources, confirming the low optical depths of the $^{13}\text{CO}(1-0)$ emission.

Assuming a filling factor of unity, the observed brightness temperature can be used to calculate the excitation temperature of the $^{12}\text{CO}(1-0)$ line. The optical depths obtained previously mean that the main line is highly optically thick so that it does not enter in the excitation temperature calculation (see e.g. Eq. 88 of Mangum & Shirley 2015) but also that the $^{13}\text{CO}(1-0)$ column density is almost independent of τ_{13} ; but we need to assume that the excitation temperatures are the same (or known) for both isotopologues as in Yuan et al. (2016). The excitation tempera-

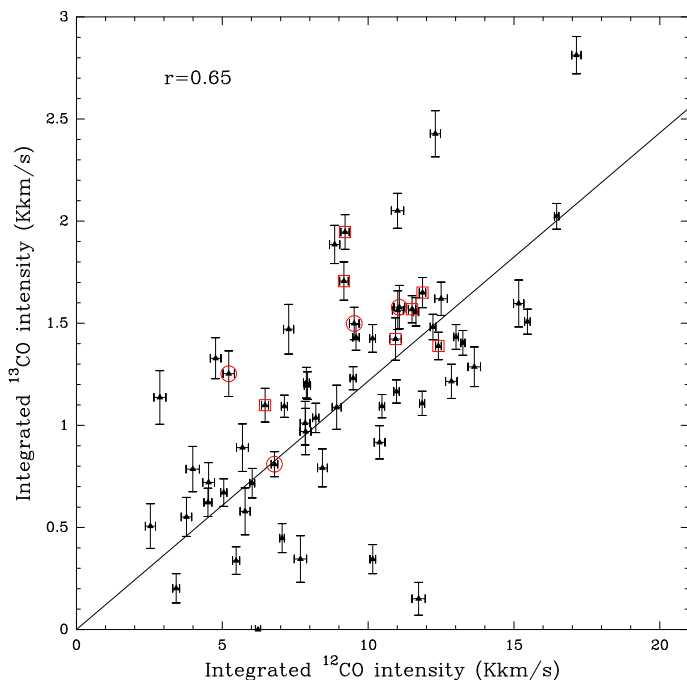


Fig. 10. Integrated intensities of ^{12}CO and ^{13}CO lines for all positions observed. The line indicates the best-fit: $I_{^{13}\text{CO}} = \frac{I_{^{12}\text{CO}}}{8}$. Class I and II sources are indicated by respectively red circles and squares.

tures vary from 7.3 to 11.4 K for the nine sources, apparently reasonable values for the outer Galaxy. Table 3 shows the optical depths, excitation temperatures, CO column densities, and H_2 column density based on the ^{12}CO and ^{13}CO column density (see Sect. 4.5). Table 4 provides the limits to the $\text{C}^{18}\text{O}(1-0)$ emission, obtained by averaging C^{18}O and ^{13}CO spectra over the maps.

However, as explained in Shirley (2015), the effective critical density is lower than the standard value for highly optically thick lines such as $^{12}\text{CO}(1-0)$ but not the optically thin $^{13}\text{CO}(1-0)$. As a result, we expect that our hypothesis of equal excitation temperatures is inappropriate and we test lower excitation temperatures for $^{13}\text{CO}(1-0)$, halfway between the CMB temperature and the $^{12}\text{CO}(1-0)$ excitation temperature $T_{\text{ex},13} = T_{\text{bg}} + 0.5(T_{\text{ex},12} - T_{\text{bg}})$, so that the $^{13}\text{CO}(1-0)$ alternative excitation temperatures range from 5 to 7 K. While ad hoc, this preserves the order among the sources and remains sufficiently far from T_{bg} that the column density is not close to diverging. The results with the modified excitation temperature are also given in Table 3.

One may also wonder whether it is reasonable to assume the same filling factor for the two lines, as we expect there to be a low-density region near the edge of the cloud where ^{12}CO is present (self-shielded) but not ^{13}CO . This is likely the case but the external radiation field in these extreme outer galaxy sources is very low so the difference in filling factors should be small. Filling factors are extremely structure-dependent and hence very difficult to estimate, so we have not attempted to change the equal filling factor assumption for $^{13}\text{CO}(1-0)$.

4.2. Molecular column densities: HCN(1-0)

For LTE excitation, which is expected given that the energy levels are so close, the optically thin hyperfine line ratios should be 5:3:1 (i.e. 0.6 and 0.2 when compared to the main line) due to the degeneracies of the levels ($2F+1$), such that the total HCN

line strength is 1.8 times that of the main component. Figure 8 shows the HFS line ratios expected as a function of the optical depth of the main line. Cases of "anomalous" line ratios exist but these *all* result in a high $\frac{(0-1)}{(2-1)}$ ratio (Kwan & Scoville 1975; Guilloteau & Baudry 1981) and generally involve high optical depth and/or double-peaked profiles. The $(F = 1 \rightarrow 1)/(F = 2 \rightarrow 1)$ and $(F = 0 \rightarrow 1)/(F = 2 \rightarrow 1)$ line ratios for clouds 21, 56, and 57 are respectively 0.57 and 0.21, 0.60 and 0.18, 0.69 and 0.325. These values are indicated on Figure 8 and indicate that the HCN emission from clouds 21 and 56 is optically thin ($\tau \lesssim 0.5$) but cloud 57 has an optical depth $\tau \sim 1$. The agreement is excellent between the two line ratios for all three clouds.

An independent estimate can be obtained by following Yuan et al. (2016) who use the CLASS³ hyperfine structure method to fit the three lines of the summed spectra of clouds 21, 56, and 57. In addition to velocity and velocity width, this method estimates the optical depth of the main line. The optical depths obtained are $\tau_{21} = 0.24 \pm 0.15$, $\tau_{56} = 0.66 \pm 0.10$, $\tau_{57} = 1.50 \pm 1.47$ for clouds 21, 56, and 57 respectively, in good agreement with the previous estimates.

Note that because these are line ratios of the same molecule at essentially the same energy, the optical depths are those after taking into account any filling factor, i.e. *not* beam-averaged. The "naïve" and CLASS estimates are consistent with optically thin ($\tau < 1$) HCN emission from clouds 21 and 56 and $\tau \approx 1$ in cloud 57.

Optically thin means we can estimate the column density from the line intensity. If we assume that the HCN excitation temperature is that of CO, then the column densities range from $3 \times 10^{10} \text{cm}^{-2}$ to $2 \times 10^{11} \text{cm}^{-2}$ (cloud 57). If we assume that the HCN excitation temperature is between the CMB temperature and that of CO (see previous section for ^{13}CO), then the column densities are a factor 3 higher, ranging from 10^{11}cm^{-2} to $7 \times 10^{11} \text{cm}^{-2}$ (cloud 57). Yuan et al. (2016) assume a very low excitation temperature, where $T_{\text{ex}} = 2hB/k$ (the first energy level, 4.25 K for HCN), and this yields much higher HCN column densities. These column densities are beam-averaged because they use the integrated intensities, unlike the optical depths calculated earlier from the HFS ratios. The column densities for the three excitation temperatures are provided in Table 3 but our fiducial value is the intermediate one.

4.3. Molecular column densities: dense gas filling factor

Because we have an estimate of the optical depth, we can estimate the filling factor by re-arranging Eq. 2 of Yuan et al. (2016) as follows

$$T_r = \frac{h\nu}{k} [J(T_{\text{ex}}) - J(T_{\text{bg}})] \tau f \quad (1)$$

where $J(T) = [\exp(h\nu/kT) - 1]^{-1}$ which becomes

$$f = \frac{kT_r}{h\nu\tau} [J(T_{\text{ex}}) - J(T_{\text{bg}})]^{-1} \quad (2)$$

We use the optically thin approximation $(1 - \exp(-\tau)) \approx \tau$ but at the moderate optical depths present here this has little effect. We can then use the values of τ to deduce a limit for the filling factor f for the two T_{ex} above.

In order to apply this reasoning to the other sources, we can average the 3 optical depths obtained from the CLASS fits. We obtain $\langle \tau \rangle \approx 0.53$ when weighting either by the inverse of the

³ <https://www.iram.fr/IRAMFR/GILDAS/>

uncertainty or by the square of the inverse of the uncertainty. We apply this to the weaker sources which were not mapped, hence probably over-estimating τ . The filling factors obtained range from 4-16% for our fiducial HCN(1-0) excitation temperature, see Table 3. Wang et al. (2020) found dense gas filling factors of 6-28% in the molecular filament GMF54 (Ragan et al. 2014) over the regions where ^{13}CO was detected (equally our case), so the values we find appear reasonable. GMF54 is beyond the molecular ring and few appropriate comparison sources are available. We then expect the true (not beam-averaged) column densities to be a factor $1/f$ times higher (col. 10 divided by col 14 in Table 3). This yields HCN column densities for the cores of $\approx 2 \times 10^{12} \text{ cm}^{-2}$ except for clouds 56 and 57 which may reach 10^{13} cm^{-2} . Note that this is for the total line width and not per km s^{-1} and assumes that the dense gas occupies a relatively small fraction of the beam.

4.4. Molecular column densities: HCO^+ (1-0)

HCO^+ is believed to be less abundant than HCN (Godard et al. 2010; Watanabe et al. 2017) and the turbulent linewidths and dipole moments are similar such that if HCN is optically thin, then HCO^+ should be as well. Taking HCO^+ to be optically thin, we can do the same calculations, again assuming our fiducial excitation temperature midway between T_{bg} and $T_{\text{ex,CO}}$ (Sect 4.1). The column densities are given in Table 3. We can see that overall the HCN and HCO^+ column densities are similar: $0.4 < \frac{N_{\text{HCN}}}{N_{\text{HCO}^+}} < 2$ (see columns 10 and 13 of Table 3).

Having established that the HCN(1-0) line, and likely the HCO^+ line, are optically thin or nearly so, we can ask ourselves whether the apparently similar HCN and HCO^+ column densities necessarily reflect the true abundance ratio. The critical density of HCN is about 7 times higher than that of HCO^+ (see Shirley 2015, Table 1 or, for HCO^+ , Fig. 3 extrapolating to our column densities), potentially resulting in more severely subthermal excitation for the HCN line. This could reduce the HCN line intensities, from which we estimate the column densities, more than the HCO^+ , such that the true HCN/ HCO^+ abundance ratio could be higher. As it is difficult analytically, the following section will explore this more quantitatively via non-LTE calculations.

4.5. Molecular column densities: H_2

Observations of ^{12}CO (1-0), ^{13}CO (1-0), HCN(1-0), and HCO^+ (1-0) have been presented. The latter two molecules are considered dense gas tracers as their critical densities are about 100 times higher than for CO where $n_{\text{crit}} \approx 1000 \text{ cm}^{-3}$ and less when highly optically thick. We can estimate the average H_2 column density from the CO observations by simply dividing by the fractional abundance (Pineda et al. 2013; Fontani et al. 2012), such that $N(\text{H}_2) = N(^{12}\text{CO})/\chi_{^{12}\text{CO}}$ or $N(\text{H}_2) = N(^{13}\text{CO})/\chi_{^{13}\text{CO}}$ where the column densities are given in columns 5 and 8 of Table 3. The $N(\text{H}_2)$ values are presented in the last two columns of Table 3. The H_2 column densities derived in this way are significantly higher than when using the standard large-scale $N(\text{H}_2)/I_{\text{CO}}$ factor used in extragalactic observations (e.g. Bolatto et al. 2013). This is expected as the CO emission from the outer galaxy is weak compared to the inner galaxy (Sodroski et al. 1995; Digel et al. 1994), presumably due to lower abundances and lower temperatures. Extragalactic observations by Sandstrom et al. (2013) found that the $N(\text{H}_2)/I_{\text{CO}}$ ratio did not change significantly within the inner disk (out to 0.7

R_{25}). However, the positions observed here are far beyond R_{25}^4 and the ratios we find by dividing the $N(\text{H}_2)$ from Table 3 by I_{CO} from Table 1 are still within the scatter of their Figure 4, such that there is no conflict.

Rather standard values of $N(\text{H}_2)$ are found, of order $10^{22} \text{ H}_2 \text{ cm}^{-2}$, suggesting that the procedure is reasonable and that outer galaxy, even extreme outer galaxy, molecular clouds have similar masses and column densities as local clouds. Taking the maps in Figures 4, 5, and 6 as representative of the size of the clouds, we obtain sizes of 10–15 pc. If the depth is the same, the average density (i.e. for a volume filling factor of unity) is $< n > \approx 10^{22}/3 \times 10^{19} \approx 300 \text{ cm}^{-3}$. This is sufficient to thermalize the highly optically thick ^{12}CO (1-0) line but not the HCN or HCO^+ . In order to reach densities where the dense gas tracers are excited, either the cloud would be a thin sheet with a line-of-sight depth about 1% of the extent perpendicular to the line of sight, or the HCN and HCO^+ emission is produced by dense clumps within the cloud which do not contribute significantly ($> 10\%$) to the cloud mass or the ^{12}CO (1-0) emission. We will assume the latter.

It is difficult to estimate the H_2 column density of the dense clumps as the HCN and HCO^+ abundances are not well known. HCN sticks to dust and is thus less abundant in cool dense environments. Lahuis & van Dishoeck (2000) suggest that the HCN abundance with respect to H_2 is $\chi_{\text{HCN}} \approx 10^{-8}$ and higher in hot environments. In the outer Galaxy clouds, we are clearly not in the "hot environment" case. A study of Planck cold cores by Yuan et al. (2016) found very low abundances, roughly 1.5×10^{-10} for both HCN and HCO^+ . Although these clouds were generally much closer, with an average distance of 1.3 kpc, this work has the physical conditions closest to the outer disk observations presented here. The Fontani et al. (2022) and Patra et al. (2022) sources (massive star-forming regions) are very different (although in the outer disk) with broader lines, outflows, strong HCN and HCO^+ emission and even H^{13}CN emission; they do not estimate abundances. Pirogov et al. (1995) find an HCN abundance $\chi_{\text{HCN}} > 10^{-10}$ towards a high-latitude cloud. Turner et al. (1997) estimate $\chi_{\text{HCN}} > 10^{-9}$ from observations of translucent molecular clouds. Watanabe et al. (2012) and Watanabe et al. (2017) find $\chi_{\text{HCN}} \approx 10^{-9}$ towards a low-mass class 0 protostar and $\chi_{\text{HCN}} \approx 2 \times 10^{-9}$ towards W 51 respectively. In their extragalactic work, Gao & Solomon (2004a) assume $\chi_{\text{HCN}} = 2 \times 10^{-8}$. Watanabe et al. (2014) observed two positions in M 51 and find fractional abundances $\chi_{\text{HCN}} \approx 10^{-9}$. Martín et al. (2006) and Aladro et al. (2011) find values within a factor two of 10^{-9} for respectively NGC 253 and M 82 such that the column density of dense gas is:

$$N(\text{H}_2)_{\text{dense}} = 10^{21} \times \frac{N_{\text{HCN}}}{10^{12}} \times \frac{10^{-9}}{\chi_{\text{HCN}}} \times \frac{1}{f} \text{ cm}^{-2} \quad (3)$$

where N_{HCN} is the beam averaged value but, because we divide by the filling factor f , $N(\text{H}_2)_{\text{dense}}$ is the estimated $N(\text{H}_2)$ of the dense clumps. Note that this expression keeps the HCN abundance as a free parameter but introduces reasonable values in order to provide an illustrative value of the H_2 column density. The range of χ_{HCN} that we regard as likely in the extreme outer disk environment is $10^{-9} \gtrsim \chi_{\text{HCN}} \gtrsim 10^{-10}$.

⁴ Estimates of the disk mass scale length of the Galaxy range between 2 and 3 kpc (Binney & Vasiliev 2023; Bovy & Rix 2013) and following Gusev et al. (2012) we estimate the blue-band scale length to be about 3.5 kpc, yielding $R_{25} \approx 11 \text{ kpc}$ assuming a central disk surface brightness of $21.65 \text{ mag}''^{-2}$ from Freeman (1970).

A beam averaged HCN or HCO^+ column density of a few 10^{11} cm^{-2} (Table 3 cols. 10 and 13) corresponds to beam-averaged dense gas column of $N(\text{H}_2)_{\text{dense}} \approx 10^{21} \text{ cm}^{-2}$, to be compared with $N(\text{H}_2) \approx 10^{22} \text{ cm}^{-2}$ from cols. 15 and 16 of Table 3. Thus, depending on the abundance, the mass in the clumps dense enough to excite the HCN and HCO^+ molecules represents of order 10% of the mass.

5. Physical conditions via radiative transfer calculations

The analytical calculations in the previous section are necessarily based on the hypothesis that the molecules are in Local Thermal Equilibrium. LTE is a strong assumption which is probably not valid, particularly for high-dipole moment molecules like HCN and HCO^+ . We made a first attempt to account for this by allowing for a lower excitation temperature for the optically thin (or nearly so) molecular emission. In this section we make non-LTE calculations in order to go a step further and in particular to treat the HCN and HCO^+ molecules separately because although they both have high dipole moments, their critical densities are different and the non-LTE transfer calculations enable us to interpret the factor ~ 2 difference in intensity.

5.1. Model setup

To constrain the volume and column densities of our observed outer Galaxy clouds, we have run a grid of non-LTE models of the HCN and HCO^+ line emission using the radiative transfer program RADEX⁵ (van der Tak et al. 2007). This program solves for the relative populations of the rotational energy levels of the molecules, taking collisional and radiative (de-)excitation into account, and treats the line radiative transfer with an escape probability formalism. The free parameters in the calculation are the kinetic temperature, the gas density, and the molecular column density. In the calculations, we assume a background temperature of 2.73 K, a turbulent line width of 1.0 km s^{-1} , and a uniform medium without velocity gradients. The linewidths of these clouds are slightly above 1.0 km s^{-1} and any column density per turbulent linewidth should be multiplied by the linewidth (Table 2) to obtain the total column density.

Watanabe et al. (2017) indicate that $\chi_{\text{HCO}^+} \approx \chi_{\text{HCN}}/3$ on average in the sources they consider (their Figures 10, 11), with $\chi_{\text{HCO}^+} \lesssim 10^{-9}$. Although somewhat uncertain, we take this abundance ratio for our calculations. The decreasing [N/O] ratio would favor HCO^+ in the outer disk but HCO^+ requires a source of ionization. The competition between these effects is difficult to evaluate and, to our knowledge, model calculations have not provided insight to this. Based on the estimates in Yuan et al. (2016), we see no evidence for lower HCO^+/HCN abundance ratios.

Spectroscopic data for the HCN and HCO^+ rotational and hyperfine structure were taken from the Cologne Database for Molecular Spectroscopy (CDMS)⁶ (Müller et al. 2005). The HCO^+ calculations use collision data with H_2 by Flower (1999), which cover rotational levels up to $J=20$ and temperatures of 40–200 K. For the collisional (de)excitation of the lowest rotation-hyperfine levels of HCN with H_2 , two calculations exist, which both cover our relevant energy levels (up to $J=8-10$) and temperatures (down to 5 K and up to 30–100 K), but which differ in the ratio between the rates for radiative ($\Delta J=1$) and

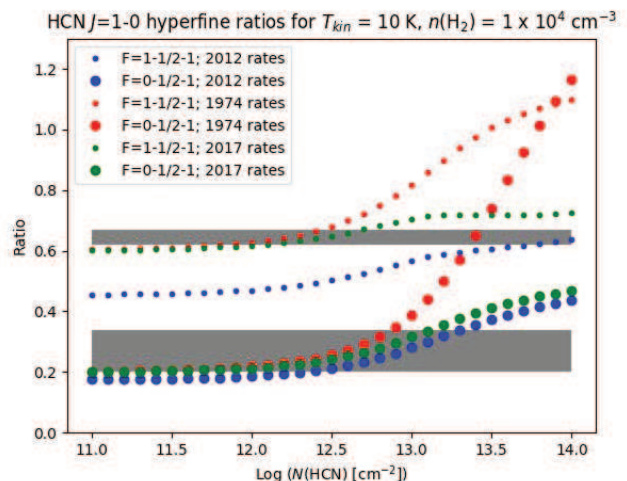


Fig. 11. Intensity ratios of the hyperfine components of the HCN $J=1-0$ line, calculated with RADEX as a function of $N(\text{HCN})$. Grey areas indicate observed ranges for the $F=1-1/2-1$ (top) and $0-1/2-1$ (bottom) ratios, respectively 0.6, 0.6, 0.7 and 0.2, 0.2, 0.3 for clouds 21, 56, and 57. The numbers indicating the rates refer to the years of publication of the rates.

non-radiative ($\Delta J=0$, $\Delta F=0, \mp 1$) transitions. The calculation by Ben Abdallah et al. (2012) used a potential energy surface for the interaction with a reduced dimensionality, averaging over H_2 orientations, and found that collisional deexcitation through non-radiative (cross- F) channels is $\approx 10\times$ faster than through $\Delta J=1$ channels. However, after upgrading the close coupling calculations to full dimensionality, Hernández Vera et al. (2017) found that the collisional deexcitation through both types of channels proceeds at approximately equal rates. For comparison, the quasi-classical calculation by Green & Thaddeus (1974) did not resolve the hyperfine structure of HCN and used He as collision partner. The corresponding datafile on the Leiden Atomic and Molecular Database (LAMDA) (Schöier et al. 2005)⁷ assumes that the radiative transitions have equal collision rates, while the cross- F rates are zero. For lack of experimental data on the relative propensities of cross- F rates, we have explored all 3 sets of collision rates in our models for HCN.

5.2. Model results

To constrain the column densities of the clouds, we model the intensity ratios of the hyperfine components of the HCN $J=1-0$ transition. Figure 11 shows the result for an assumed T_{kin} of 10 K and $n(\text{H}_2) = 10^4 \text{ cm}^{-3}$, and calculations for T_{kin} in the 10–30 K range and $n(\text{H}_2)$ in the $10^3-3 \times 10^4 \text{ cm}^{-3}$ range indicate that our results depend only weakly on the assumed gas density and kinetic temperature. Column densities of $N(\text{HCN}) \approx 3 \times 10^{12} \text{ cm}^{-2}$ are seen to be consistent with both observed ratios (indicated by the grey areas), but only if the Hernández Vera et al. (2017) collision data with the similar cross- F and cross- J rates are used. Using the data with the large cross- F rates, there is no column density of HCN which matches both observed ratios simultaneously. The collision data with the cross- F rates equal to zero are also able to match the observed hyperfine ratios, but the inferred $N(\text{HCN})$ is less reliable since these hyperfine collision rates were assumed rather than calculated. These rates also lead to unrealistically high hyperfine ratios toward high HCN column densi-

⁵ <https://personal.sron.nl/~vdtak/radex/index.shtml>

⁶ <http://cdms.de>

⁷ <http://home.strw.leidenuniv.nl/~moldata/>

Cloud	I_{HCO^+} K km s ⁻¹	V_{HCO^+} km s ⁻¹	$\text{fwhm}_{\text{HCO}^+}$ km s ⁻¹	I_{HCN} K km s ⁻¹	V_{HCN} km s ⁻¹	fwhm_{HCN} km s ⁻¹	rms mK
7	0.148 ± 0.015	-102.89 ± 0.07	1.484 ± 0.181	0.022 ± 0.018	-102.92 ± 0.18	0.494 ± 0.779	17
14	0.133 ± 0.015	-101.11 ± 0.08	1.407 ± 0.178	0.023 ± 0.008	-101.28 ± 0.06	0.373 ± 0.135	19
16	0.072 ± 0.012	-99.69 ± 0.09	1.161 ± 0.250	0.031 ± 0.010	-99.36 ± 0.09	0.615 ± 0.249	18
18	0.117 ± 0.013	-99.40 ± 0.09	1.616 ± 0.192	0.046 ± 0.010	-99.87 ± 0.21	1.628 ± 0.365	12
30	0.100 ± 0.013	-104.02 ± 0.09	1.297 ± 0.181	0.058 ± 0.014	-104.48 ± 0.17	1.246 ± 0.245	22
34	0.201 ± 0.018	-107.25 ± 0.09	2.221 ± 0.255	0.038 ± 0.012	-107.17 ± 0.18	1.143 ± 0.386	17
21	0.553 ± 0.018	-101.10 ± 0.03	1.801 ± 0.073	0.086 ± 0.012	-101.20 ± 0.08	1.020 ± 0.166	19
sum	2 – 1			0.067 ± 0.006	-101.35 ± 0.05	1.276 ± 0.136	3.4
sum	1 – 1			0.038 ± 0.009	-96.53 ± 0.16	1.321 ± 0.402	3.4
sum	0 – 1			0.014 ± 0.008	-108.32 ± 0.24	0.827 ± 0.624	3.4
56	0.319 ± 0.013	-103.55 ± 0.05	2.345 ± 0.107	0.126 ± 0.013	-103.45 ± 0.09	1.828 ± 0.239	12
sum	2 – 1			0.096 ± 0.009	-103.57 ± 0.08	1.794 ± 0.189	4.3
sum	1 – 1			0.058 ± 0.013	-98.73 ± 0.19	1.744 ± 0.448	4.3
sum	0 – 1			0.017 ± 0.011	-110.70 ± 0.37	1.126 ± 0.761	4.3
57	0.474 ± 0.016	-102.23 ± 0.03	2.013 ± 0.082	0.133 ± 0.016	-102.17 ± 0.09	1.463 ± 0.200	16
sum	2 – 1			0.083 ± 0.009	-102.37 ± 0.10	1.799 ± 0.236	5.9
sum	1 – 1			0.057 ± 0.012	-97.38 ± 0.19	1.821 ± 0.446	5.9
sum	0 – 1			0.027 ± 0.014	-109.59 ± 0.51	1.980 ± 1.116	5.9

Table 2. Results of observations of central positions, deduced from gaussian fits. Intensities are in main beam scale but for HCN are only of the main $F = 2 \rightarrow 1$ transition. The spectra for clouds 21, 56, and 57 have been summed (see Fig. 7 and the lines marked "sum" provide the fits to the individual hyperfine components. The expected velocity differences are 4.842 and -7.064 km s⁻¹ with respect to the main (2-1) component. The satellite lines were fit using as initial guess (for the fit algorithm of CLASS) the main line velocity + 4.842 or -7.064 for the 1 – 1 and 0 – 1 transitions respectively. That the velocities do not show exactly these differences provides an independent estimate of the uncertainty in the velocity determination. Rms noise levels are in mK converted to main beam scale and per 0.2 km s⁻¹ channel.

Cl	T_{CO}	$\chi_{12/13}$	$T_{\text{ex,CO}}$	N_{CO}^a 10 ¹⁷	$N_{^{13}\text{CO}}^a$ 10 ¹⁵	$T_{\text{ex},^{13}\text{CO}}^b$	$N_{^{13}\text{CO}}^b$ 10 ¹⁵	N_{HCN}^a 10 ¹¹	N_{HCN}^b 10 ¹¹	N_{HCN}^c 10 ¹¹	$N_{\text{HCO}^+}^a$ 10 ¹¹	$N_{\text{HCO}^+}^b$ 10 ¹¹	f^b %	$N(\text{H}_2)^a$ log	$N(\text{H}_2)^b$ log
	K		K	cm ⁻²	cm ⁻²	K	cm ⁻²	cm ⁻²	cm ⁻²	cm ⁻²	cm ⁻²	cm ⁻²			
7	5.4	93.20	8.75	1.82	1.17	5.74	4.23	0.29	0.91	2.91	0.63	2.01	5.8	21.67	22.00
14	4.5	93.67	7.80	2.83	1.71	5.27	6.33	0.40	1.28	3.04	0.75	2.43	7.2	21.87	22.19
16	4.0	93.20	7.30	2.52	1.74	5.02	6.48	0.63	2.07	4.10	0.48	1.57	10.9	21.81	22.19
18	5.4	92.73	8.75	1.96	1.35	5.74	4.87	0.60	1.91	6.09	0.50	1.59	12.1	21.69	22.06
30	5.0	102.13	8.35	0.58	1.61	5.54	5.88	0.84	2.71	7.68	0.47	1.53	16.4	21.28	22.29
34	5.8	105.42	9.15	2.08	1.24	5.94	4.45	0.45	1.41	5.03	0.77	2.44	9.3	21.87	22.23
21	8.0	95.55	11.40	0.96	0.89	7.06	3.04	0.55	1.66	9.84	1.32	4.03	12.3	21.42	21.90
56	6.0	127.04	9.35	3.14	1.91	6.04	6.81	1.45	4.58	17.18	1.16	3.68	8.6	22.31	22.75
57	5.5	125.63	8.85	2.98	1.16	5.79	4.18	2.27	7.23	23.72	1.96	6.26	4.0	22.27	22.52

Table 3. Temperatures, column densities, and filling factors as described in Section 4. Col. 2 is the observed CO line temperature, col. 3 the radially varying $^{12/13}\text{CO}$ abundance ratio, col. 4 is the CO excitation temperature, and columns 5 and 6 are the deduced CO and ^{13}CO column densities, all following Sect. 3.2 of Yuan et al. (2016). Col. 7 is our fiducial excitation temperature for the optically thin or close to thin species (see Sect. 4.1). Columns 8 - 13 are the column densities derived using the excitation temperatures from Sect. 4.1 and Yuan et al. (2016), see footnotes below. Col. 14 is the estimated filling factor from Sect. 4.3. The H_2 column densities in the last two columns are derived as in the first paragraph of Sect. 4.5, where col. 16. is the H_2 column deduced from the ^{13}CO line assuming an excitation temperature as in (b) below. (a) Assumes all excitation temperatures are those derived for CO (col. 4). (b) Our fiducial case which attempts to account for subthermal excitation temperatures such that $T_{\text{ex}} = T_{bg} + 0.5 \times (T_{\text{ex,CO}} - T_{bg})$. (c) Follows Yuan et al. (2016) hypothesis where HCN and HCO^+ excitation temperatures are equal to $2hB/k$.

Cloud	^{13}CO K km s ⁻¹	C^{18}O K km s ⁻¹	ratio	$\chi_{13/18}$
21	0.60 ± 0.06	0.03 ± 0.06	$\geq 20 \pm 10$	9.6
56	1.39 ± 0.07	0.20 ± 0.07	$\geq 7.0 \pm 2$	10.3
57	0.85 ± 0.06	0.11 ± 0.06	$\geq 7.7 \pm 3$	10.3

Table 4. $^{13}\text{CO}(1-0)$ and $\text{C}^{18}\text{O}(1-0)$ intensities averaged over the maps. $\chi_{13/18}$ is the ^{13}CO to C^{18}O abundance ratio at the galactocentric distance of the cloud, which for optically thin emission and equal excitation temperatures would be the intensity ratio. The last two columns can legitimately be compared.

by the hyperfine ratios. We conclude that the HCN line emission indicates $N(\text{HCN}) \approx 3 \times 10^{12} \text{ cm}^{-2}$, using the collision data by Hernández Vera et al. (2017).

To constrain the volume densities of the clouds, we model the ratios of the HCN and HCO^+ $J=1-0$ lines. These calculations assume $T_{\text{kin}} = 20 \text{ K}$ and an abundance ratio of $[\text{HCN}]/[\text{HCO}^+] = 3$ (Watanabe et al. 2017). Figure 12 shows the result as calculated with RADEX using the HCN collision rates by Hernández Vera et al. (2017). Our observed line ratio of $\approx 1/2$ (summed over the HCN hyperfine components) is seen to correspond to H_2 densities in the 10^3 – 10^4 cm^{-3} range. The analytical calculations in the previous section yielded similar HCN and HCO^+ columns but the degree of subthermal excitation could not be assessed. Nonetheless, if $\chi_{\text{HCO}^+} > \chi_{\text{HCN}}/3$, then a higher

ties. The models also reproduce the observed absolute intensities of the HCN lines, for similar column densities as indicated

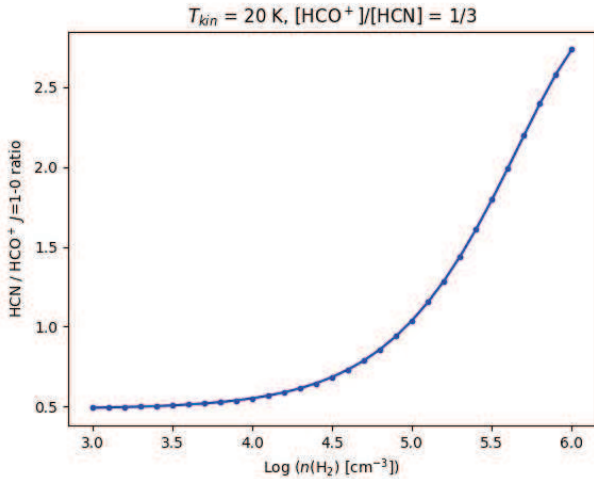


Fig. 12. Intensity ratio of the HCN and HCO⁺ $J=1-0$ lines, calculated with RADEX as a function of $n(\text{H}_2)$.

density would be required to yield the observed HCN/HCO⁺ line ratio. For example, if $\chi_{\text{HCO}^+}/\chi_{\text{HCN}} = 0.5$ (and not 1/3), then we would deduce a density of $n(\text{H}_2) \approx 10^{4.5} \text{ cm}^{-3}$.

5.3. HCN and HCO⁺ as dense gas tracers

Depending on the HCN and HCO⁺ abundances, the H₂ column density deduced from HCN could be comparable to that deduced from the CO observations (Table 3). *Can the gas be the same?* We can test this using the intensities of the lines. Assuming that the majority of the CO emission comes from gas with a density $n \lesssim 3000 \text{ cm}^{-3}$ (see discussion in Sect. 4.5), RADEX calculations show that for $n \lesssim 3000 \text{ cm}^{-3}$, $I_{\text{HCN}}/I_{\text{CO}} \lesssim 0.001$ (H₂ column assumed is 10^{21} cm^{-2} with abundances $\chi_{\text{CO}} = 10^{-5}$ and $\chi_{\text{HCN}} = 10^{-9}$). Since $I_{\text{HCN}}/I_{\text{CO}} \gtrsim 0.01$ from Tables 1 and 2, the HCN emission does not come from the gas emitting the majority of the CO emission but rather from clumps or cores within the less dense ambient molecular gas. In principle, the CO could come from gas with $n > 3000 \text{ cm}^{-3}$. However, not only would the clouds necessarily be much thinner along the line of sight but also the ¹³CO emission would be quite unusual, much stronger in the higher- J transitions than in ¹³CO(1-0). The few data available for the ¹³CO(2-1) line, or even CO(2-1), at large scales in the outer parts of galaxies suggest that the higher- J transitions are not stronger (Sakamoto et al. 1997; Braine et al. 1993). Hence, in these outer disk clouds, HCN and HCO⁺ trace dense gas ($n > 10^3 \text{ cm}^{-3}$).

Figure 9 shows that the HCO⁺ line is on average twice as strong as the HCN line. To make this figure, the HCN(1-0) main line intensities were multiplied by 9/5 to account for the flux in the weaker satellite lines which have low signal-to-noise ratios and thus can add considerable noise to the sum of the intensities. As seen in Sect. 4, the optical depth is low so this procedure should be appropriate. Since both lines are optically thin, we have used RADEX to estimate the typical density at which the HCO⁺(1-0) is twice the total HCN(1-0) line intensity. For a column density ratio of 3, this occurs at $n \lesssim 10^4 \text{ cm}^{-3}$ ($T_{\text{kin}} = 20 \text{ K}$). If in fact the HCO⁺ abundance is higher (than 1/3 of the HCN abundance), then the density implied by the observed flux ratio is higher. A larger fraction of the HCO⁺ emission, compared to HCN, comes from the lower density CO-emitting gas and this is why the above calculation sets a lower limit to the typical density

of the dense component. This is also seen in Fig. 11 of the observations of W3(OH) by Nishimura et al. (2017) which shows that the HCN(1-0)/HCO⁺(1-0) ratio decreases towards the more extended and more diffuse material.

We obtain a typical clump or core size of $L \approx N/n$ where N is the dense gas column density defined in Eq. 3 such that

$$M_{\text{cl}} = \rho V \approx n 2m_p f_h^{-1} (N/n)^3 \quad (4)$$

where $2m_p f_h^{-1}$ is the average molecular mass. Adopting reference values of $N_{\text{HCN}} = 3 \times 10^{11} \text{ cm}^{-2}$, $n = 10^4 \text{ cm}^{-3}$, $\chi_{\text{HCN}} = 10^{-9}$, and $f = 0.1$, we can express the clump or core mass as follows by substituting Eq. 3 into Eq. 4

$$\begin{aligned} M_{\text{cl}} &= \frac{2m_p}{f_h} 10^{-8} \left(\frac{10^4}{n} \right)^2 (3 \times 10^{21})^3 \left(\frac{N_{\text{HCN}}}{3 \times 10^{11}} \right)^3 \left(\frac{10^{-9}}{\chi_{\text{HCN}}} \right)^3 \left(\frac{0.1}{f} \right)^3 \\ &= 0.62 \left(\frac{10^4}{n} \right)^2 \left(\frac{N_{\text{HCN}}}{3 \times 10^{11}} \right)^3 \left(\frac{10^{-9}}{\chi_{\text{HCN}}} \right)^3 \left(\frac{0.1}{f} \right)^3 M_{\odot} \end{aligned} \quad (5)$$

with a hydrogen fraction of $f_h = 0.73$. The mass in such a clump is of order a solar mass but highly dependent on the abundance, such that if $\chi_{\text{HCN}} = 10^{-10}$ then the clump mass becomes $620 M_{\odot}$. The other parameters are constrained by observations: N_{HCN} by the HCN flux, N_{HCN}/f by the HCN optical depth limit, and n by the HCN/HCO⁺ flux ratio.

6. Link between star formation and dense gas fraction

Gao & Solomon (2004b) suggested that the star formation rate is proportional to the mass of dense gas such that starburst galaxies have high dense gas masses. In ultraluminous IR Galaxies (ULIRGs), there is generally a huge amount of gas concentrated near the center and hence the dense gas mass (HCN flux) and fraction (typically the HCN/CO flux ratio) are high. Here we examine smaller scales so, to compare dense gas with star formation, we have compared these line ratios for positions with and without a class I or II source. The HCN/CO and HCO⁺/CO flux ratios are marginally higher for the positions with a class I or class II source but not significantly.

Aside from the good correlation between 8 μm and 24 μm emission, the main result is that the HCN/CO and HCO⁺/CO ratios are a factor two lower for the sources at high galactic latitude ($b > 2^\circ$, sources 7, 14, 16, 18, 30, and 34, see top panel of Fig. 13). These sources are identified by red triangles in Fig. 13.

In a spiral galaxy, the molecular-to-atomic gas ratio at kpc scales is largely controlled by the local hydrostatic pressure (see Blitz & Rosolowsky 2004), itself a function of the stellar and gaseous surface densities. As the stellar surface density decreases with galactocentric distance (spiral disks are approximately exponential), so does the molecular fraction. The same logic applies to the dense gas fraction which is presumably why the HCN/CO and HCO⁺/CO flux ratios we find are below the inner disk ratios (e.g. Usero et al. 2015). It likely also explains why the high-latitude clouds (200pc or more above the galactic mid-plane) of our sample or from Yuan et al. (2016) have lower HCN/CO and HCO⁺/CO flux ratios.

Far-IR emission comes mainly from dust heated by young stars and as such is a standard tracer of star formation. There is a clear correlation between the presence of star formation, as traced by Far-IR emission, and molecular line emission at large scales. We will use the Spitzer 24 μm and 8 μm emission to trace

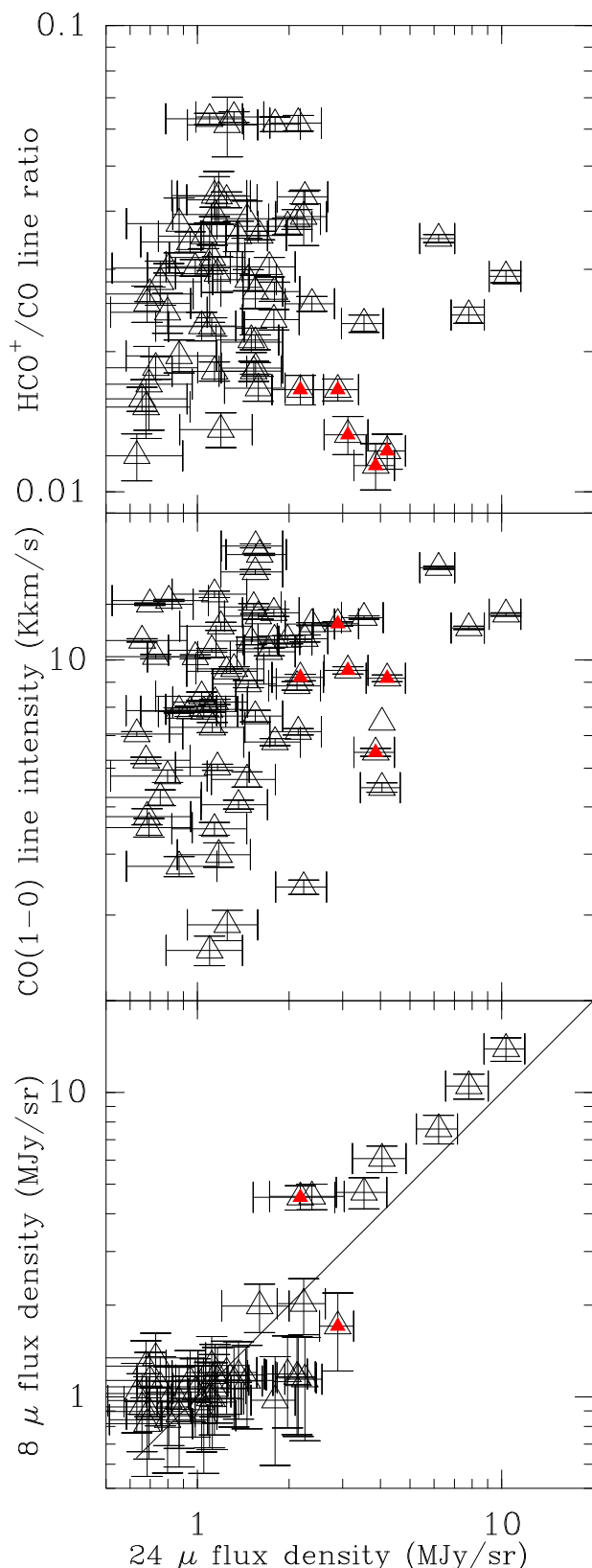


Fig. 13. Comparison of molecular line intensities and tracers of star formation. The bottom panel compares the SFR tracers: background-subtracted $24\ \mu\text{m}$ emission and $8\ \mu\text{m}$ emission, also background-subtracted (the background emission is considerably stronger than any stellar contribution at $8\ \mu\text{m}$). The middle panel shows how the ^{12}CO intensity varies with SFR. The top panel shows how the dense gas fraction, as traced by the HCO^+/CO ratio, varies with SFR. The red triangles indicate the sources which are at high galactic latitude. It should be immediately apparent that these sources are not distinguishable from the others in the lower two frames but occupy a specific region with low dense gas fraction in the top panel. Neither 8 nor $24\ \mu\text{m}$ data are available for cloud 30.

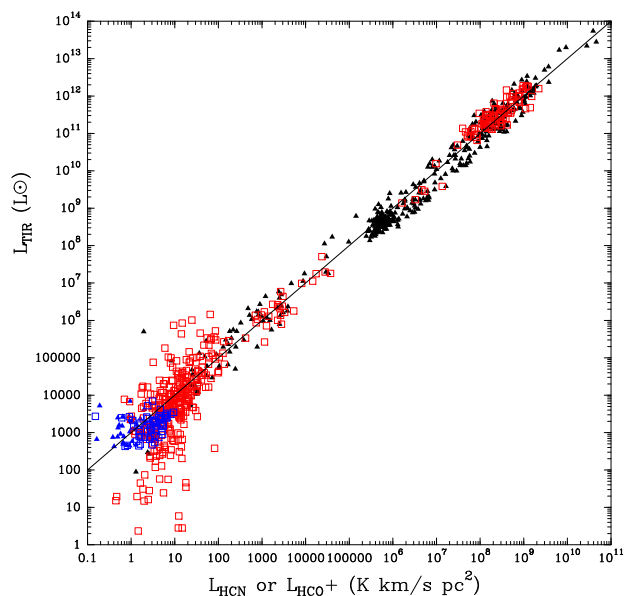


Fig. 14. Link between dense gas mass (HCN or HCO^+ luminosity on the x-axis) and star formation rate (IR luminosity on the y-axis). The line shows a linear relation with $L_{\text{FIR}}/L_{\text{HCN}}$ or $L_{\text{FIR}}/L_{\text{HCO}^+} = 1000 L_{\odot} (\text{K km s}^{-1} \text{pc}^2)^{-1}$. HCN data are shown as filled triangles and HCO^+ as open squares. The outer disk data presented in this paper are shown in blue. The sources for the data are: Chin et al. (1997), Chin et al. (1998), Gao & Solomon (2004b), Gao et al. (2007), Brouillet et al. (2005), Wu et al. (2005), Ma et al. (2013), Buchbender (2014), Krips et al. (2008), Juneau et al. (2009), Privon et al. (2015), Graciá-Carpio et al. (2008), García-Burillo et al. (2012), Chen et al. (2015), Chen et al. (2017), Usero et al. (2015).

the SFR because our sources are unobscured and the Spitzer data have high angular resolution, respectively $6''$ and $2''$. The $24\ \mu\text{m}$ emission is a standard tracer of star formation (Calzetti et al. 2007) but the $8\ \mu\text{m}$ emission varies strongly as a function of environment and particularly metallicity (Draine et al. 2007). However, for a given environment (outer disk in the present case), it can be used to trace the SFR (Boquien et al. 2015).

The $24\ \mu\text{m}$ and $8\ \mu\text{m}$ emission⁸ were background subtracted by examining a histogram of the values in the maps. The value considered to be "background" is where the number of pixels reaches about 1% of the maximum number of pixels in the histogram. Thus we are not sensitive to variations in a small number of pixels yet we use low values in the map. The 8 and $24\ \mu\text{m}$ measurements are continuum, meaning that they see all matter along the line of sight and, unlike for the spectra, outer galaxy and more local material cannot be distinguished. As we are looking in the plane of the galaxy, there is emission virtually everywhere such that the background value is not well defined. The 8 and $24\ \mu\text{m}$ fluxes provided can only be considered best estimates. Towards our clouds, with the exception of cloud 30, the outer galaxy cloud is the main source (this is deduced from the relative CO line strength at each velocity). However, along other lines of sight within the 8 and $24\ \mu\text{m}$ maps, this is not necessarily the case so we subtract a low value rather than the most common value (which reflects the emission and not the background). We make sure not to take extremely low values which could be influenced by noise. Figure 13 shows that the 8 and $24\ \mu\text{m}$ fluxes are highly correlated, which would not be the case if the estimated background fluxes were highly incorrect. The fluxes were

⁸ <https://sha.ipac.caltech.edu/applications/Spitzer/SHA>

measured with two different instruments (IRAC and MIPS on the Spitzer satellite), making a coincidence even less likely.

Figure 13 shows how the molecular line intensity varies as a function of the SFR. Not all sources have both 24 μm and 8 μm available so, after showing that the 24 μm and 8 μm fluxes are highly correlated ($r = 0.82$, bottom panel), we trace the SFR with the 24 μm fluxes but use 8 μm fluxes when no 24 μm data are available. The CO intensities are weakly correlated with SFR ($r \approx 0.2$, middle panel) and the HCN and HCO⁺ intensities (not shown in Fig. 13) are not significantly correlated with SFR. The HCO⁺/CO ratio (top panel), tracing the dense gas fraction, is not significantly correlated with SFR but the sources further than 300 pc above the galactic plane stand out as having very low HCO⁺ (and HCN, not shown) emission. These sources do not stand out in other ways.

Comparing to larger scales, the dense gas tracers (or dense gas mass following Gao & Solomon 2004b), and star formation rate, as calculated from the 8 or 24 μm flux (Boquien et al. 2010; Galametz et al. 2013), follow the extrapolation of the trends found in Chen et al. (2015) and Shimajiri et al. (2017), as shown in Fig. 14. The reason for the absence of a correlation between L_{HCN} and SFR is likely the similarity of the regions we observe, all occupying the same area of Fig. 14.

7. Comparison with other environments

In the extreme outer Galaxy clouds observed here, the line intensity ratios are approximately: CO/HCN ~ 70 , CO/HCO⁺ ~ 35 , and CO/¹³CO ~ 7.5 . Thus, the CO emission is stronger relative to the other lines than in the majority of sources observed thus far (see e.g. Fig. 8 of Chen et al. 2015).

However, in the nearly square degree region of Orion B mapped by Gratier et al. (2017), they obtain very similar ratios for their median values of CO, ¹³CO, HCO⁺, and HCN, although the HCN emission is stronger after correction for flux in the satellite lines. The median values tend to sample the more extended lower column density regions, as also found recently by Evans et al. (2020).

The Shimajiri et al. (2017) work on nearby molecular clouds showed that HCN and HCO⁺ emission often traced star formation while the H¹³CN and H¹³CO⁺ lines were sensitive to the total H₂ column. These regions are much denser than the outer Galaxy clouds studied here and the HCN and HCO⁺ emission is highly optically thick. The net effect is that the intensity of HCN and HCO⁺ is highly dependent on gas temperature (thus star formation) rather than density. In the highest column density regions, the main isotope lines are strongly self-absorbed. HCN emission in outer Milky Way clouds is optically thin and does not trace star formation and so it appears akin to the H¹³CN in Shimajiri et al. (2017), which traces column density in high volume density regions. While Shimajiri et al. (2017) do not calculate H¹³CN abundances, the H¹³CO⁺ abundances are within a rather narrow range: $1.5 - 5.8 \times 10^{-11}$ with respect to H₂. These values are consistent with $\chi_{\text{HCO}^+} \sim 10^{-9}$ and the column densities ($N_{\text{H}^{13}\text{CO}^+} \sim 10^{12} \text{ cm}^{-2}$) are similar to our estimates for the main isotope.

Yuan et al. (2016) present HCN and HCO⁺ observations, also with the PMO telescope, of cool clumps identified by the Planck satellite. They are at approximately the solar circle (mean distance of 1.3 kpc), neither outer nor inner Milky Way. Their estimated column densities are variable but have median N_{HCN} and $N_{\text{HCO}^+} \approx 10^{12} \text{ cm}^{-2}$, although the ratio is quite variable. Their abundance estimates differ from source to source but are mostly

$\chi \sim 10^{-10}$ for both HCN and HCO⁺. Other Galactic works include Park et al. (1999) and Barnes et al. (2011) who assume higher abundances, typically $\chi \sim 10^{-9}$. In the cool clouds, the HCO⁺ line is stronger than HCN.

So far we have compared with other Galactic observations but extragalactic sources allow for a much greater range in properties. A relatively distant region in M 51 was observed with the IRAM interferometer by Chen et al. (2017) who found HCN/CO ratios similar to ours but generally higher HCN/HCO⁺ ratios. M 31 was observed by Brouillet et al. (2005) and, in the outer parts, a similarly low HCN/CO ratio was found but again a higher HCN/HCO⁺ ratio. The Large Magellanic Cloud (LMC) provides an environment with a lower metallicity and a higher radiation field than our observations of the outer Milky Way but at similar scales. Chin et al. (1997) observed several lines in the LMC and found again that the HCO⁺ emission was stronger than the HCN (or HNC), unlike large Milky Way molecular clouds or star-forming galaxies (their Table 10). Subsequently, Nishimura et al. (2016), Anderson et al. (2014), Galametz et al. (2020), and Seale et al. (2012) observed CO-strong molecular clouds in the LMC and consistently confirm the weak emission from Nitrogen-bearing molecules, as well as strong CCH emission. Braine et al. (2017) observed the low-metallicity galaxies M 33, IC 10, and NGC 6822 in the local group and found ratios quite similar to those presented here. These authors concluded that the low HCN/HCO⁺ ratio was due to weak HCN emission rather than particularly strong HCO⁺ emission. This was attributed to the decrease in N/O with metal deficiency.

The low HCN/HCO⁺ ratios we observe in the extreme outer Galaxy are probably due to a combination of low volume density and subsolar metallicity. A gradient in N/O exists in the Galaxy (Magrini et al. 2018). However, while Arellano-Córdova et al. (2021) find a N/O gradient of $-0.015 \text{ dex kpc}^{-1}$ from optical observations, Rudolph et al. (2006) find a N/O gradient of $-0.03 \text{ dex kpc}^{-1}$ from Far-IR spectral line data. As a result, the N/O ratio for the distant clouds should be approximately half of the solar circle value. If the new values underestimate the gradient, then the low HCN fluxes could be entirely due to a decrease in abundance. Two features lead us to believe that volume density is also an issue. First of all, the new gradient uses high-quality GAIA DR2 distances. Secondly, the low molecular fraction in and the diffuse nature of the outer parts of spiral galaxies argues for a lower hydrostatic pressure as compared to the inner disk (see e.g. Blitz & Rosolowsky 2004). While the molecular line ratios are not clearly related to the level of star formation, there is a clear difference between the clouds in the plane and those at $b > 2^\circ$ in that the HCO⁺/CO ratio is lower for the latter (Fig. 13, but also HCO⁺/¹³CO and the same ratios with HCN). Our clouds at higher latitude are at $h \gtrsim 300 \text{ pc}$ from the galactic plane such that the local pressure should be lower.

We find a similar effect in the Yuan et al. (2016) sample. Clouds with $h > 180 \text{ pc}$ above the plane have significantly lower average and median $I_{\text{HCO}^+}/N(^{13}\text{CO})$ and $I_{\text{HCN}}/N(^{13}\text{CO})$ values than the clouds at $h < 180 \text{ pc}$. The mean values are 50% higher in the plane and the median is twice as high for both $I_{\text{HCO}^+}/N(^{13}\text{CO})$ and $I_{\text{HCN}}/N(^{13}\text{CO})$. $N(^{13}\text{CO})$ has been used as the reference column density but the higher dense fraction (stronger HCN and HCO⁺ emission) close to the Galactic plane is equally found using the ¹²CO column density (see Table 3 of Yuan et al. 2016).

8. Conclusions

The dense gas tracers HCN(1-0) and HCO⁺(1-0) were observed in a sample of extreme outer Galaxy clouds ($15 \lesssim R_{\text{gal}} \lesssim 21 \text{ kpc}$)

from the Sun et al. (2015) unbiased CO survey. The clouds were chosen for their reasonably strong CO ($I_{CO} > 7 \text{ km s}^{-1}$) and ^{13}CO ($I_{^{13}\text{CO}} > 1.4 \text{ km s}^{-1}$) emission. None were detected in $\text{C}^{18}\text{O}(1-0)$ but the limits are close to what would be expected for optically thin emission so far out in the disk.

1. The HCN and HCO^+ emission is weak, both in an absolute sense and relative to the CO lines (Tables 1 and 2). $I_{\text{HCO}^+} \approx 0.03 I_{\text{CO}} \approx 0.21 I_{^{13}\text{CO}} \approx 2 I_{\text{HCN}}$ after accounting for the satellite HCN lines. These ratios are typical of a subsolar metallicity environment, where N is more affected than O.

2. The $^{12}\text{CO}(1-0)$ emission is highly optically thick but the $^{13}\text{CO}(1-0)$ is optically thin, $\tau_{13} \lesssim 1$. The estimated H_2 column densities are $\sim 10^{22} \text{ cm}^{-2}$, depending on the hypotheses (Table 3), but in all cases several times higher than would be deduced from a standard extragalactic $N(\text{H}_2)/I_{\text{CO}} \sim 2 \times 10^{20} \text{ cm}^{-2}/(\text{K km s}^{-1})$ conversion factor (e.g. Bolatto et al. 2013).

3. The lines are narrow and the hyperfine ratios of HCN indicate that the emission is optically thin, $\tau_{\text{HCN}(1-0)} \lesssim 1$. We obtain beam-averaged HCN column densities, for our fiducial excitation temperature, of $1 - 7 \times 10^{11} \text{ cm}^{-2}$ (Table 3, col 10). With the optical depths, we can estimate the dense gas filling factor, again dependent on the assumed T_{ex} , and we obtain values of $10 \pm 6\%$ (Table 3), in reasonable agreement with other estimates. Other molecules and transitions can trace gas substantially denser, which would then have a lower filling factor. Similar results are obtained for the HCO^+ line (see Table 3).

4. The H_2 volume densities required to collisionally excite the optically thin HCN and HCO^+ lines are about 100 times those required to excite the CO lines. Hence, see Sect. 4.5, we conclude that the HCN and HCO^+ emission does not trace the bulk of the gas but the denser clumps. Combined with the derived filling factors, and dependent on the assumed but poorly known abundances of HCN and HCO^+ , we estimate (Sect. 4.5) that the gas emitting the $\text{HCN}(1-0)$ and $\text{HCO}^+(1-0)$ flux represents some 10% of the total gas mass.

5. The critical densities of HCN and HCO^+ are not the same and we use RADEX non-LTE models to obtain estimates of the HCN column density and use the HCN/HCO^+ intensity ratio to constrain the volume density of the "dense" gas. Because these lines are optically thin, the intensity ratio depends on the abundance ratio. For $\chi_{\text{HCO}^+} = \chi_{\text{HCN}}/3$ (Watanabe et al. 2017), the "dense" gas is likely $n(\text{H}_2) \lesssim 10^4 \text{ cm}^{-3}$ but if the relative HCO^+ abundance is higher, as obtained in Section 4, then denser gas is required for the same line ratio.

6. As part of the modeling, it was realized that the high cross-F rates initially found by Ben Abdallah et al. (2012) could not fit our data but that the revised rates by Hernández Vera et al. (2017) provided a good fit. It was thus possible to observationally test hyperfine collision rates.

7. The original motivation was to explore the link between star formation and dense gas in the poorly known outer disk environment. Our data fall on the general $L_{\text{HCN}} - L_{\text{IR}}$ plot (Fig. 14) but, within our sample, there is no correlation between the SFR, as traced by the 8 and/or $24 \mu\text{m}$ flux, and the flux in the HCN and HCO^+ lines or the dense gas fraction as traced by the HCN/CO or HCO^+/CO line ratios. Instead, we find that the dense gas fraction decreases away from the galactic plane, presumably due to lower pressure. An analysis of the Yuan et al. (2016) sources reveals the same trend.

Acknowledgements. We would like to dedicate this work to our dear friend and colleague Prof. Yu Gao, who passed away during the revision of the article. We would like to thank the DeLingHa telescope staff and the Purple Mountain Observatory for making these observations possible. JB would like to thank Nan-

Jing University for hosting. We would also like to acknowledge grants from the french PNC and the ANR program for financing through the ANR-11-BS56-010 project STARFICH. Y.S. acknowledges support by the Youth Innovation Promotion Association, CAS (Y2022085), *Light of West China* Program, CAS (No. xzbzg-zdsys-202212), and the NSFC through grant 11773077. HC is supported by Key Research Project of Zhejiang Lab?No. 2021PE0AC0. Y.G. was supported by the National Key Basic Research and Development Program of China (2017YFA0402700), the National Natural Science Foundation of China (11861131007, U1731237, 12033004), and Chinese Academy of Sciences Key Research Program of Frontier Sciences (QYDZJSSW-SLH008). This publication makes use of data products from the Wide-field Infrared Survey Explorer, which is a joint project of the University of California, Los Angeles, and the Jet Propulsion Laboratory/California Institute of Technology, funded by the National Aeronautics and Space Administration.

References

- Aladro, R., Martín, S., Martín-Pintado, J., et al. 2011, *A&A*, 535, A84
 Anderson, C. N., Meier, D. S., Ott, J., et al. 2014, *ApJ*, 793, 37
 Arellano-Córdova, K. Z., Esteban, C., García-Rojas, J., & Méndez-Delgado, J. E. 2021, *MNRAS*, 502, 225
 Barnes, P. J., Yonekura, Y., Fukui, Y., et al. 2011, *ApJS*, 196, 12
 Ben Abdallah, D., Najjar, F., Jaidane, N., Dumouchel, F., & Lique, F. 2012, *MNRAS*, 419, 2441
 Binney, J. & Vasiliev, E. 2023, *MNRAS*
 Blitz, L. & Rosolowsky, E. 2004, *ApJL*, 612, L29
 Bolatto, A. D., Wolfire, M., & Leroy, A. K. 2013, *ARA&A*, 51, 207
 Boquien, M., Calzetti, D., Aalto, S., et al. 2015, *A&A*, 578, A8
 Boquien, M., Calzetti, D., Kramer, C., et al. 2010, *A&A*, 518, L70+
 Bovy, J. & Rix, H.-W. 2013, *ApJ*, 779, 115
 Braine, J., Combes, F., & van Driel, W. 1993, *A&A*, 280, 451
 Braine, J., Shimajiri, Y., André, P., et al. 2017, *A&A*, 597, A44
 Brouillet, N., Muller, S., Herpin, F., Braine, J., & Jacq, T. 2005, *A&A*, 429, 153
 Buchbender, C. 2014, PhD thesis, Universidad de Granada, <http://hdl.handle.net/10481/31707>
 Calzetti, D., Kennicutt, R. C., Engelbracht, C. W., et al. 2007, *ApJ*, 666, 870
 Chen, H., Braine, J., Gao, Y., Koda, J., & Gu, Q. 2017, *ApJ*, 836, 101
 Chen, H., Gao, Y., Braine, J., & Gu, Q. 2015, *ApJ*, 810, 140
 Chin, Y.-N., Henkel, C., Millar, T. J., Whiteoak, J. B., & Marx-Zimmer, M. 1998, *A&A*, 330, 901
 Chin, Y.-N., Henkel, C., Whiteoak, J. B., et al. 1997, *A&A*, 317, 548
 Digel, S., de Geus, E., & Thaddeus, P. 1994, *ApJ*, 422, 92
 Draine, B. T., Dale, D. A., Bendo, G., et al. 2007, *ApJ*, 663, 866
 Evans, Neal J., I. 1999, *ARA&A*, 37, 311
 Evans, Neal J., I., Kim, K.-T., Wu, J., et al. 2020, *ApJ*, 894, 103
 Fang, M., Kim, J. S., van Boekel, R., et al. 2013, *ApJS*, 207, 5
 Flower, D. R. 1999, *MNRAS*, 305, 651
 Fontani, F., Colzi, L., Bizzocchi, L., et al. 2022, *A&A*, 660, A76
 Fontani, F., Giannetti, A., Beltrán, M. T., et al. 2012, *MNRAS*, 423, 2342
 Freeman, K. C. 1970, *ApJ*, 160, 811
 Galametz, M., Kennicutt, R. C., Calzetti, D., et al. 2013, *MNRAS*, 431, 1956
 Galametz, M., Schrubba, A., De Breuck, C., et al. 2020, *A&A*, 643, A63
 Gallagher, M. J., Leroy, A. K., Bigiel, F., et al. 2018, *ApJ*, 858, 90
 Gao, Y., Carilli, C. L., Solomon, P. M., & Vanden Bout, P. A. 2007, *ApJL*, 660, L93
 Gao, Y. & Solomon, P. M. 2004a, *ApJS*, 152, 63
 Gao, Y. & Solomon, P. M. 2004b, *ApJ*, 606, 271
 García-Burillo, S., Usero, A., Alonso-Herrero, A., et al. 2012, *A&A*, 539, A8
 Glover, S. C. O. & Clark, P. C. 2012, *MNRAS*, 426, 377
 Godard, B., Falgarone, E., Gerin, M., Hily-Blant, P., & de Luca, M. 2010, *A&A*, 520, A20
 Graciá-Carpio, J., García-Burillo, S., Planesas, P., Fuente, A., & Usero, A. 2008, *A&A*, 479, 703
 Gratier, P., Bron, E., Gerin, M., et al. 2017, *A&A*, 599, A100
 Green, S. & Thaddeus, P. 1974, *ApJ*, 191, 653
 Guilleoteau, S. & Baudry, A. 1981, *A&A*, 97, 213
 Gusev, A. S., Guslyakova, S. A., & Khramtsova, M. S. 2012, *Astronomical and Astrophysical Transactions*, 27, 233
 Hernández Vera, M., Lique, F., Dumouchel, F., Hily-Blant, P., & Faure, A. 2017, *MNRAS*, 468, 1084
 Hoekstra, H., van Albada, T. S., & Sancisi, R. 2001, *MNRAS*, 323, 453
 Jiménez-Donaire, M. J., Bigiel, F., Leroy, A. K., et al. 2019, *ApJ*, 880, 127
 Juneau, S., Narayanan, D. T., Moustakas, J., et al. 2009, *ApJ*, 707, 1217
 Kalberla, P. M. W. & Kerp, J. 2009, *ARA&A*, 47, 27
 Kennicutt, R. C., J. 1989, *ApJ*, 344, 685
 Kennicutt, R. C. & Evans, N. J. 2012, *ARA&A*, 50, 531
 Kepley, A. A., Leroy, A. K., Frayer, D., et al. 2014, *ApJL*, 780, L13
 Koenig, X. P., Leisawitz, D. T., Benford, D. J., et al. 2012, *ApJ*, 744, 130

- Krips, M., Neri, R., García-Burillo, S., et al. 2008, *ApJ*, 677, 262
- Kutner, M. L. & Ulich, B. L. 1981, *ApJ*, 250, 341
- Kwan, J. & Scoville, N. 1975, *ApJL*, 195, L85
- Lahuis, F. & van Dishoeck, E. F. 2000, *A&A*, 355, 699
- Linsky, J. L. 2003, *Sp.Sci.Rev.*, 106, 49
- Ma, B., Tan, J. C., & Barnes, P. J. 2013, *ApJ*, 779, 79
- Magrini, L., Vincenzo, F., Randich, S., et al. 2018, *A&A*, 618, A102
- Mangum, J. G. & Shirley, Y. L. 2015, *PASP*, 127, 266
- Martín, S., Mauersberger, R., Martín-Pintado, J., Henkel, C., & García-Burillo, S. 2006, *ApJS*, 164, 450
- Molinari, S., Schisano, E., Elia, D., et al. 2016, *A&A*, 591, A149
- Müller, H. S. P., Schlöder, F., Stutzki, J., & Winnewisser, G. 2005, *Journal of Molecular Structure*, 742, 215
- Nishimura, Y., Shimonishi, T., Watanabe, Y., et al. 2016, *ApJ*, 818, 161
- Nishimura, Y., Watanabe, Y., Harada, N., et al. 2017, *ApJ*, 848, 17
- Park, Y. S., Kim, J., & Minh, Y. C. 1999, *ApJ*, 520, 223
- Patra, S., Evans, Neal J., I., Kim, K.-T., et al. 2022, *AJ*, 164, 129
- Pedicelli, S., Bono, G., Lemasle, B., et al. 2009, *A&A*, 504, 81
- Pineda, J. L., Langer, W. D., Velusamy, T., & Goldsmith, P. F. 2013, *A&A*, 554, A103
- Pirogov, L., Zinchenko, I., Lapinov, A., Myshenko, V., & Shul'Ga, V. 1995, *A&AS*, 109, 333
- Privon, G. C., Herrero-Illana, R., Evans, A. S., et al. 2015, *ApJ*, 814, 39
- Ragan, S. E., Henning, T., Tackenberg, J., et al. 2014, *A&A*, 568, A73
- Reid, M. J., Menten, K. M., Brunthaler, A., et al. 2014, *ApJ*, 783, 130
- Rudolph, A. L., Fich, M., Bell, G. R., et al. 2006, *ApJS*, 162, 346
- Sakamoto, S., Hasegawa, T., Handa, T., Hayashi, M., & Oka, T. 1997, *ApJ*, 486, 276
- Sandstrom, K. M., Leroy, A. K., Walter, F., et al. 2013, *ApJ*, 777, 5
- Schmidt, T. M., Bigiel, F., Klessen, R. S., & de Blok, W. J. G. 2016, *MNRAS*, 457, 2642
- Schöier, F. L., van der Tak, F. F. S., van Dishoeck, E. F., & Black, J. H. 2005, *A&A*, 432, 369
- Schuller, F., Menten, K. M., Contreras, Y., et al. 2009, *A&A*, 504, 415
- Seale, J. P., Looney, L. W., Wong, T., et al. 2012, *ApJ*, 751, 42
- Shan, W. L., Yang, J., & Shi, S. C., et al. 2012, *ITST*, 2, 593
- Shimajiri, Y., André, P., Braine, J., et al. 2017, *A&A*, 604, A74
- Shirley, Y. L. 2015, *PASP*, 127, 299
- Skrutskie, M. F., Cutri, R. M., Stiening, R., et al. 2006, *AJ*, 131, 1163
- Sodroski, T. J., Odegard, N., Arendt, R. G., et al. 1997, *ApJ*, 480, 173+
- Sodroski, T. J., Odegard, N., Dwek, E., et al. 1995, *ApJ*, 452, 262
- Sun, Y. 2015, PhD thesis, Purple Mountain Observatory, Chinese Academy of Sciences
- Sun, Y., Xu, Y., Yang, J., et al. 2015, *ApJL*, 798, L27
- Turner, B. E., Pirogov, L., & Minh, Y. C. 1997, *ApJ*, 483, 235
- Usero, A., Leroy, A. K., Walter, F., et al. 2015, *AJ*, 150, 115
- van der Tak, F. F. S., Black, J. H., Schöier, F. L., Jansen, D. J., & van Dishoeck, E. F. 2007, *A&A*, 468, 627
- Wang, Y., Beuther, H., Schneider, N., et al. 2020, *A&A*, 641, A53
- Watanabe, Y., Nishimura, Y., Harada, N., et al. 2017, *ApJ*, 845, 116
- Watanabe, Y., Sakai, N., Lindberg, J. E., et al. 2012, *ApJ*, 745, 126
- Watanabe, Y., Sakai, N., Sorai, K., & Yamamoto, S. 2014, *ApJ*, 788, 4
- Wouterloot, J. G. A. & Brand, J. 1989, *A&AS*, 80, 149
- Wright, E. L., Eisenhardt, P. R. M., Mainzer, A. K., et al. 2010, *AJ*, 140, 1868
- Wu, J., Evans, II, N. J., Gao, Y., et al. 2005, *ApJ*, 635, L173
- Wu, J., Evans, II, N. J., Shirley, Y. L., & Knez, C. 2010, *ApJS*, 188, 313
- Yuan, J., Wu, Y., Liu, T., et al. 2016, *ApJ*, 820, 37